J. Fluid Mech. (2021), *vol*. 929, A9, doi:10.1017/jfm.2021.845

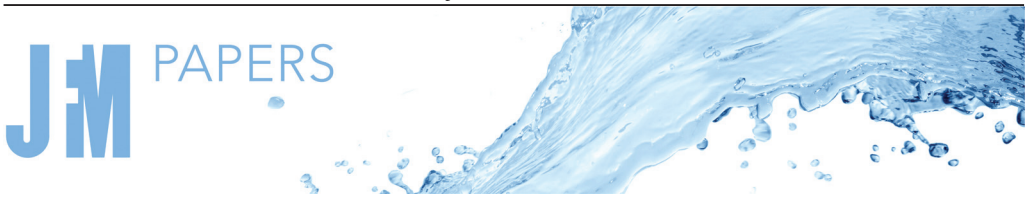

The structure of a highly decelerated axisymmetric turbulent boundary layer

N. Agastya Balantrapu[1], Christopher Hickling[1], W. Nathan Alexander[1] and William Devenport[1],†

[1]Department of Aerospace and Ocean Engineering, Virginia Tech, Blacksburg, VA 24060, USA

(Received 28 September 2020; revised 27 July 2021; accepted 22 September 2021)

Experiments were performed over a body of revolution at a length-based Reynolds number of 1.9 million. While the lateral curvature parameters are moderate ($\delta/r_s < 2$, $r_s^+ > 500$, where δ is the boundary layer thickness and r_s is the radius of curvature), the pressure gradient is increasingly adverse ($\beta_C \in [5\text{–}18]$ where β_C is Clauser's pressure gradient parameter), representative of vehicle-relevant conditions. The mean flow in the outer regions of this fully attached boundary layer displays some properties of a free-shear layer, with the mean-velocity and turbulence intensity profiles attaining self-similarity with the 'embedded shear layer' scaling (Schatzman & Thomas, *J. Fluid Mech.*, vol. 815, 2017, pp. 592–642). Spectral analysis of the streamwise turbulence revealed that, as the mean flow decelerates, the large-scale motions energize across the boundary layer, growing proportionally with the boundary layer thickness. When scaled with the shear layer parameters, the distribution of the energy in the low-frequency region is approximately self-similar, emphasizing the role of the embedded shear layer in the large-scale motions. The correlation structure of the boundary layer is discussed at length to supply information towards the development of turbulence and aeroacoustic models. One major finding is that the estimation of integral turbulence length scales from single-point measurements, via Taylor's hypothesis, requires significant corrections to the convection velocity in the inner 50 % of the boundary layer. The apparent convection velocity (estimated from the ratio of integral length scale to the time scale), is approximately 40 % greater than the local mean velocity, suggesting the turbulence is convected much faster than previously thought. Closer to the wall even higher corrections are required.

Key words: boundary layer structure, aeroacoustics

1. Introduction

Turbulent boundary layers growing over axially symmetric bodies, such as the fuselage of some aircraft or marine vehicles, are very common and have been the focus of many

† Email address for correspondence: devenport@vt.edu

past research efforts (Glauert & Lighthill 1955; Rao 1967; Patel, Nakayama & Damian 1974; Lueptow, Leehey & Stellinger 1985; Huang *et al.* 1992; Neves, Moin & Moser 1994; Snarski & Lueptow 1995; Piquet & Patel 1999; Cipolla & Keith 2003; Tutty 2008; Jordan 2014; Manovski, Giacobello & Jacquemin 2014; Kumar & Mahesh 2018*a*; Manovski *et al.* 2020). Understanding the fundamental mechanisms and the interaction of these layers with the environment is important as they are a source of significant drag, noise and structural vibrations. Particularly, these boundary layers are often ingested by rotors, generating both tonal and broadband sound known as turbulence ingestion noise (Glegg & Devenport 2017), which is a growing concern due to the imminent abundance of short-haul urban air transportation and uninhabited underwater vehicles.

Most research in axisymmetric boundary layers has considered axial flow past a constant-radius circular cylinder, excluding any streamwise pressure gradient effects. The impact of the lateral curvature on the flow has been commonly characterized by two parameters, (i) δ/r_s, the ratio of boundary layer thickness to radius of curvature, and (ii) $r_s^+ = r_s u_\tau/\nu$, the radius-based Reynolds number, where u_τ and ν are the skin-friction velocity and kinematic viscosity respectively. Three flow regimes have been reported based on these parameters, (i) large r_s^+ and large δ/r_s, corresponding to a high Reynolds number flow over a long slender rod; (ii) small r_s^+ and large δ/r_s, corresponding to an axially symmetric wake with an inner layer due to the wall; and (iii) large r_s^+ and small δ/r_s, corresponding to the high Reynolds number flow over a large cylinder (Piquet & Patel 1999). The first two regimes, with significant curvature effects, have been extensively studied with their relevance to towed array sensor systems (Lueptow *et al.* 1985; Cipolla & Keith 2003). The third regime representing practical, vehicle-relevant conditions, has received comparatively less attention. Though this flow regime is relatively similar to the flat-plate boundary layer, many important effects are still observed, such as higher skin friction and fuller velocity profiles due to increased transverse mixing. The turbulence intensity away from the surface is lower compared with the flat-plate case, due to the relatively fuller mean-velocity profiles (Piquet & Patel 1999; Kumar & Mahesh 2018*a*). However, the fundamental structure of the turbulence has been shown to remain very similar to the flat-plate counterpart, except the enhanced large-scale activity due to the less-constrained motion, as a result of the relatively smaller surface area (Neves *et al.* 1994; Snarski & Lueptow 1995). For a detailed summary, refer to Jordan (2014).

However, studies on axisymmetric boundary layers under streamwise pressure gradients are relatively limited, focusing mostly on the mean flow in the adverse pressure gradient (APG) region or nearly separating flows, and downstream wake (Dengel & Fernholz 1990; Hammache, Browand & Blackwelder 2002; Jimenez, Hultmark & Smits 2010; Kumar & Mahesh 2018*b*; Manovski *et al.* 2020). This is not surprising, since planar pressure gradient flows themselves are complex and under active investigation. Generally, the flow structure is sensitive to the Reynolds number, local pressure gradient and the upstream history (Bobke *et al.* 2017), posing a prohibitively large parameter space. Despite such a challenge several aspects have been clarified, including an increased mean-velocity defect in the outer region, and a corresponding increase in the turbulence activity, manifesting as a secondary peak in the turbulence stresses, that amplifies and drifts away from the wall with increasing pressure gradient (Nagano, Tsuji & Houra 1998; Kitsios *et al.* 2017). Several studies on the turbulence structure of APG layers have attributed this to the increased importance of large-scale motions (of the order of boundary layer thickness) in the outer region. For example, Vila *et al.* (2017) have shown that the first four modes of a moderately decelerated boundary layer, estimated through proper orthogonal decomposition, accounted for 40 % of the turbulent kinetic energy, and captured both the

magnitude and location of the outer peak in the Reynolds streamwise normal stress and shear-stress profile. While the details are, of course, sensitive to the flow history and local parameters, these large-scale motions in the outer layer (log region and above) have been shown to strongly interact with the small-scale motions closer to the wall, modulating both the amplitude and frequency (Harun *et al.* 2013; Drozdz & Elsner 2017; Lee 2017).

Questions regarding the impact of APG on the growth and organization of the large-scale motions in the outer region have been partly answered, with Skåre & Krogstad (1994) and Maciel, Simens & Gungor (2017) observing the sweeping motions to be stronger and to occur more frequently than ejections, compared with their equal probability for the zero pressure gradient (ZPG) case. Lee (2017) – in his direct numerical simulation (DNS) of mild ($\beta_C = (\delta_1/\tau_w)\,\mathrm{d}p/\mathrm{d}x = 0.72$), moderate ($\beta_C = 2$) and strong ($\beta_C = 9$) APG layers – observed the characteristics of the energized large-scale motions to be very sensitive to the severity of APG. While the spanwise length scale of the conditional u' (streamwise velocity)-structures increased monotonically with the pressure gradient, the streamwise length scale did not; the streamwise scale was longer for weak APG ($\beta_C < 2$) but was significantly shorter at stronger APG, shorter even in comparison with the ZPG case. By analysing both the instantaneous and conditional structures, he observed that the streamwise hairpin structures actively concatenated into larger motions at mild APG, but were generally more separated and less coherent, resulting in reduced concatenation for stronger APG. Additionally, he observed this suppression of the hairpin vortex packets to be associated with increased importance of the conditional roll modes – that were centred in the outer layer and corresponded to sweeps and ejections – in organizing the overall flow. Overall, this is indicative of a fundamental change in the turbulence structure as the boundary layer experiences a strong APG.

Indeed, both experimental (Skåre & Krogstad 1994) and DNS studies (Gungor *et al.* 2016; Kitsios *et al.* 2017) investigating large-defect boundary layers have observed a new secondary peak in the turbulence kinetic energy production, dissipation and transfer, collocated with the peak in the turbulent stress profiles. Furthermore, some of these studies have also observed the mean-velocity profiles to be inflectional at the same location that generally indicate inviscid instability, prompting Kitsios *et al.*; Gungor *et al.* to suggest some resemblance to free-shear flows. While the inflectional profiles have been observed in previous experimental studies as well (Elsberry *et al.* 2000; Song, DeGraaff & Eaton 2000), recent investigation by Schatzman & Thomas (2017) has revealed some strong evidence for the resemblance to free-shear flows. They considered an unsteady boundary layer on a ramp with an upper airfoil that imposed unsteadiness through plasma actuation. Through quadrant analysis of the phase-averaged shear-stress profiles, measured with a laser Doppler anemometer, they observed ejections to dominate above the inflection point and sweeping motions to dominate below. This spatial organization, observed at all streamwise locations in the boundary layer, led them to hypothesize the presence of an embedded shear layer with spanwise-oriented coherent vorticity centred about the inflection point. These motions were attributed to inviscid instabilities as the Rayleigh–Fjørtoft theorem was satisfied, which requires the spanwise mean vorticity to reach a maximum at the inflection point (i.e. $U''(U - U_{IP}) < 0$, where $'$ denotes differentiation with respect to the wall-normal coordinate and U_{IP} is the velocity at the inflection point). Inspired by prior work on free-shear layers, they proposed new length and velocity scales, based on the shear and velocity at the inflection point. With these scales and a coordinate system centred about the inflection point, the mean-velocity and turbulence intensity profiles over a significant streamwise extent were found to collapse. While this is certainly encouraging, there are several outstanding questions. For instance,

the instantaneous flow is not expected to 'see' the mean-velocity profile, and therefore the occurrence of inflectional instabilities is debatable. Although Schatzman & Thomas find that the Rayleigh–Fjørtoft theorem is satisfied at the outer inflection point, which is considered a necessary and generally sufficient condition for the presence of inviscid instabilities, Maciel *et al.* (2017) find no evidence for the coherent structures indicative of such an instability, Kelvin–Helmholtz or varicose. Furthermore, this hypothesis is not compatible with the occurrence of an outer peak in the Reynolds stresses even in the absence of inflection points, as in the flow of Maciel *et al.* (2018). This gives rise to a conjecture that the inflectional velocity profiles and the outer turbulence peaks are simply correlated, without sharing a cause-and-effect relationship. In any case, further investigation into this requires a systematic study over a broad range of pressure gradients and is outside our scope. Here, our interest is to examine whether the embedded shear layer scaling is valid for an axisymmetric body, with a vehicle-relevant configuration (with an axial variation in the transverse curvature and axial pressure gradient), and if so, to observe the implications for the turbulence and correlation structure, from a perspective of providing information to support the turbulence modelling and aeroacoustic predictions.

It is important to mention that, from a broader perspective of developing a framework for non-equilibrium APG flows, there are several outstanding issues, many of which are discussed by Maciel *et al.* (2018). For example, the layer structure of APG flows, as to a clear definition of 'outer' vs 'inner' regions; a consistent choice of parameters to quantify the various forces; and a parameter to represent the flow history, require a continuation of sustained effort, meticulous experiments and rigorous analysis.

To conclude, axisymmetric boundary layers with moderate curvature parameters but strong axial pressure gradient – that represent practical, vehicle-relevant conditions – are not understood due to the inherent complications posed by axial pressure gradient. The relative importance of the different aspects, and the validity of some of the recent developments in APG flows must be examined with respect to mean flow, turbulence and correlation structure. The present study aims to fill some of these gaps through experiments over a body of revolution, with the key objectives being:

(i) to reveal the physics of an axisymmetric boundary layer with a practical flow history, examining both the mean flow and the turbulence structure, and in part, examine the embedded shear layer hypothesis;
(ii) to provide the experimental dataset for validation of numerical simulations for relatively high Reynolds number, APG flows;
(iii) to provide new quantitatively usable insight into the correlation structure as needed to define the source terms for turbulence ingestion noise prediction and other flow acoustic problems.

2. Apparatus and instrumentation

2.1. *Wind tunnel*

This study was performed in the Virginia Tech Stability Wind Tunnel, a low-speed closed-circuit facility with an interchangeable test section that is 7.32 m long, with a 1.85 m $\times$ 1.85 m cross-section. All measurements were made in the anechoic test section, where the sidewalls are formed by tensioned Kevlar 120 fabric that remains acoustically transparent while containing the flow. These sidewalls are flanked by anechoic chambers lined with 0.610 m acoustic foam wedges to absorb the transmitted sound down to 190 Hz. The floor and ceiling of the test section are comprised of 0.61 m square metal perforate

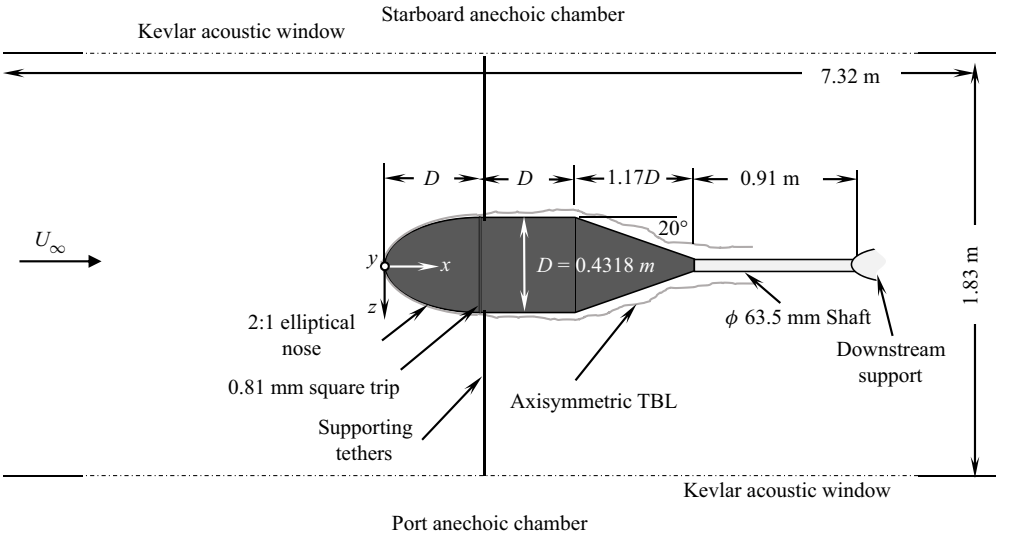

Figure 1. Schematic of the top view of the test section, showing the BOR geometry and experimental arrangement.

panels covered by Kevlar, and backed by acoustic foam wedges. This facility can achieve speeds of up to 80 m s^{-1}, and the flow in the empty test section is closely uniform, with a free-stream turbulence intensity of 0.016 % at 12 m s^{-1} that increases to 0.034 % at 57 m s^{-1}. An exchange tower behind the fan is used to regulate the temperature in the tunnel with the atmospheric ambient. The detailed aerodynamic and aero-acoustic performance of this facility has been documented by Devenport *et al.* (2013).

2.2. *Body of revolution (BOR)*

The BOR geometry, shown in figure 1, was inspired by prior work on a body of revolution with an aft ramp designed to have a Stratford–Smith pressure distribution (that corresponds to a boundary layer constantly on the verge of separation) (Hammache *et al.* 2002). The BOR was chosen to have a characteristic length of $D = 0.4318$ m, with a fore body comprised of a 2 : 1 semi-ellipsoid nose and a constant-diameter (D) cylindrical section, with a 0.8 mm square trip ring sandwiched at $x/D = 0.98$ (the trip was approximately 35 % of the local boundary layer thickness estimate obtained from the Thwaites–Walz method (Schetz & Bowersox 2011)). The coordinate frame used throughout this paper is shown in figure 1, and has an origin at the nose, with the x-axis along the BOR axis of symmetry, the y-axis pointing vertically upward and the z-axis towards the port wall, completing a right-handed system. The aft ramp of the BOR is a cone joined to the constant-diameter section through a sharp corner. Steady Reynolds-averaged Navier Stokes (RANS) calculations and surface oil flow visualization on a quarter-scale BOR – that set the half-apex angle at 20° – were used to ensure that the boundary layer would decelerate as rapidly as possible without separating. The tail cone was truncated at $x/D = 3.172$, with a local radius of $0.073D$, to facilitate the installation in the wind tunnel.

The BOR was fabricated in house, and is hollow, with the shell made from concentric rings of rigid-polyurethane tooling foam, supported internally by aluminium 6061 bulk

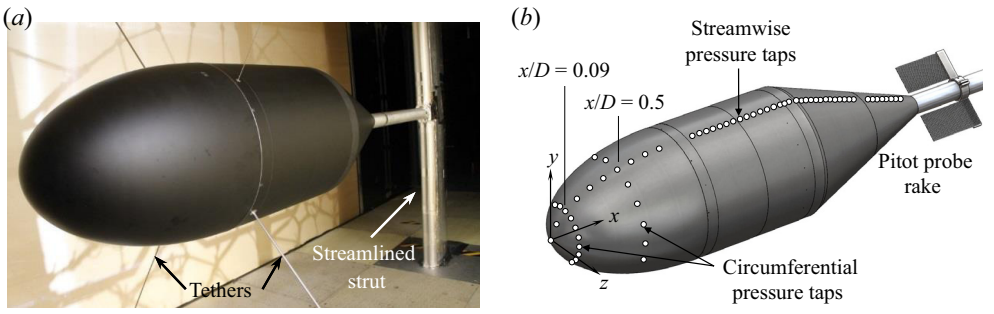

Figure 2. (*a*) Photograph of the BOR installed in the test section of the Virginia Tech Stability Tunnel. (*b*) Arrangement of 85 pressure taps on the body: 52 ports measuring the streamwise distribution, and 36 ports measuring the circumferential uniformity.

heads on either side of the constant-diameter section. The outer surface was smoothed and spray painted to ensure a seamless skin that is opaque to the flow. The entire assembly, weighing 55 kg, was suspended at the centre of the test section with a variable-tension tether system, and positioned by a downstream sting, resulting in a net blockage of 4.3 % (see figure 2*a*). The tether system consisted of cruciform tethers that were cleated to the fore bulk head inside the body, just downstream of the trip ring, forming clean, sealed, cylinder–body junctions at the points where they entered the body. These tethers ran diagonally across the test section, tensioned by manual linear stages just outside the ceiling on either side, and stabilized by 14.4 kg steel blocks on the floor side. The angle between the tethers was close to 90°, allowing precise adjustment of the body angle of attack. The tethers, initially 1.6 mm steel cables, were upgraded to 0.9 mm ones over the course of experiments. The restricted influence of these tethers on the BOR turbulence, documented with a single hot-wire anemometer, is described in § 3.1.

The hollow sting used to position the BOR at the downstream end was flush to within 1 mm with the outer skin at the BOR tail, and was connected to a streamlined strut on the downstream end. The sting was 0.91 m long, with the length set through potential flow calculation, to restrict the inviscid perturbation of the streamlined strut at the BOR tail to within 0.5 % of the tunnel free-stream velocity. Further, the downstream strut was streamlined (with polystyrene and sheet metal) to a McMaster Henderson airfoil to minimize the trailing edge shedding (see Glegg & Devenport 2017, p. 253).

2.3. *Steady pressure measurements*

Steady pressure measurements were made to examine the circumferential uniformity and document the axial distribution of the surface pressure. A total of 85 half-millimetre diameter pressure taps were embedded into the BOR: 51 ports measured the streamwise distribution of the mean surface pressure, and 36 ports measured the circumferential uniformity on the nose at $x/D = 0.095$ and 0.5 (figure 2*b*). The pressure signal was sampled at 100 Hz, via Tygon tubes, by a DTC Initium ESP-32HD acquisition system (range = 10 in. WC range, accuracy = ± 0.05 %). The body was installed at $0 \pm 0.25°$ angle of attack by iteratively adjusting the position with the tether system until the pressure measured by the circumferential arrays were uniform. The free-stream static pressure, stagnation pressure and velocity were measured from pressure taps in the wind-tunnel contraction and settling chamber 2.51 m upstream from the test-section leading edge. A thermocouple in the diffuser measured the ambient temperature.

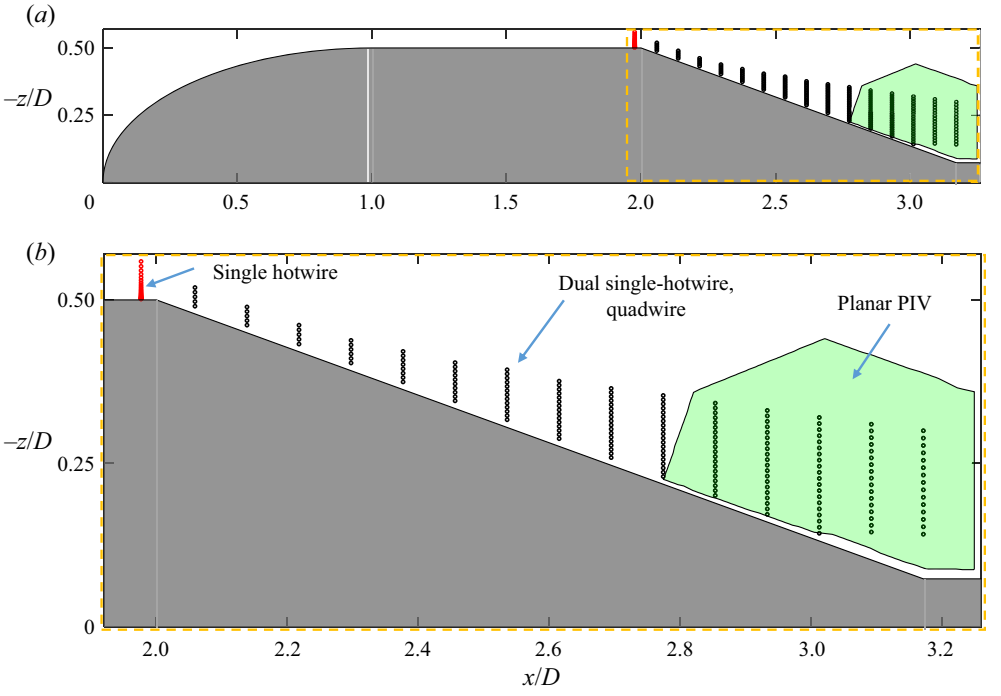

Figure 3. Schematic showing the various measurements of the turbulent velocity over the BOR.

To further confirm the circumferential uniformity, the stagnation pressure distribution at the BOR tail ($x/D = 3.172$) was measured with a custom built Pitot-probe rake. The rake consisted of a radial line of 119, 0.5 mm diameter Pitot probes positioned across the wake diameter from $r/D = 0.12$ to 0.3 on either side of the sting support (figure 2). The rake was rotated about the x-axis to 36 angular stations resolving the BOR wake profile, including the tether wakes. An Esterline 98RK-1 NetScanner system with range $= \pm 10$ in. WC and accuracy $= 0.05\,\%$ was used to measure the stagnation pressure.

2.4. *Turbulent velocity measurements*

Measurements of the turbulent velocity were made at a Reynolds number $Re_L = U_\infty L/\nu$ of 1.90×10^6, where U_∞ is the tunnel free-stream velocity and L ($= 1.3695$ m) is the BOR length; U_∞ was nominally 22 m s^{-1}, and was varied in order to maintain a constant Re_L (to within 2 %) as the tunnel temperature fluctuated. Measurements were made using a combination of constant-temperature hot-wire anemometry and particle image velocimetry (PIV), as summarized in figure 3. The inflow to the APG ramp was measured upstream of the corner, at $x/D = 1.977$, with a single hot-wire anemometer, obtaining the single-point statistics and spectra; the streamwise evolution over the ramp was documented first by two single hot-wires, followed by a four-sensor hot-wire, acquiring 15 profiles for each, between $x/D = 2.0$ to 3.172, obtaining the statistics and temporal structure. Furthermore, a subset of the two-point space–time structure of the streamwise velocity at the BOR tail were made with two single-wire probes, obtaining the radial and circumferential correlations at $x/D = 3.172$. These measurements were supplemented by non-time-resolved planar PIV, covering the rear third of the ramp $x/D = 2.80$ to 3.172,

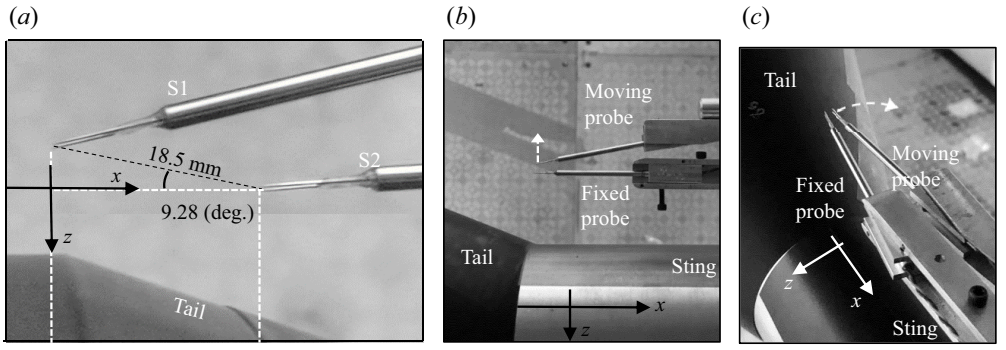

Figure 4. Velocity measurements on the BOR ramp with single hot-wire. (*a*) Dual probe arrangement on ramp to measure the single-point statistics and large-scale convection velocity. (*b*) Radial correlations at the BOR tail ($x/D = 3.172$) measured with a moving and fixed single hot-wire. (*c*) Arrangement to measure circumferential correlations at the tail.

documenting the spatial structure of the ramp flow. Further information detailing the set-up, acquisition and post-processing is discussed below.

2.4.1. *Constant-temperature hot-wire anemometry*

The inflow to the ramp was measured by a single-sensor hot-wire manufactured by Auspex Corporation (type AHWU-100, with tungsten wire of length 1.2 mm and diameter 5 μm), documenting the streamwise velocity and turbulence intensity over a 30-point profile, at a single circumferential station upstream of the corner, at $x/D = 1.977$ (figure 3). Similar measurements were made over the ramp using two similar single-sensor hot-wire probes, separated by 18.5 mm along a 9.3° inclination to the body axis (figure 4*a*), while they were traversed over 15 streamwise stations on the ramp ($x/D = 2.059$ to 3.172). While this separation ensured the upstream probe was free from downstream probe interference – providing clean single-point statistics – the dual probe arrangement was used to derive the turbulence convection velocity. The mean velocity and streamwise Reynolds stress from the upstream probe were validated against the PIV results from § 2.4.2 and shown in Appendix A. The probes were calibrated frequently in the wind tunnel to account for the temperature variation, and corrections were made following the procedure of Bearman (1971). Although the statistical random uncertainty (for 20:1 odds) is acceptable at approximately 0.5 % U_∞ for the mean velocity and 2 %U_∞ for the turbulence intensity, the bias error from rectification and axial sensitivity could be significant, especially near the wall, given a highly turbulent flow (Tutu & Chevray 1975). For example, as observed by Tutu & Chevray for a local turbulence intensity of 0.3 – which exists along the ramp in only the lower 10 % of the boundary layer – the mean velocity can be overestimated by up to 3 % and turbulence intensity can be underestimated by up to −5.7 %. Therefore the near-wall results must be interpreted with special care but are not a focus of this study. Furthermore, spatial filtering effects are not expected to be significant as the sensor length $l^+ (= lU_\tau/\nu)$ varied between 66 and 18 (see table 2). For this range of l^+, Hutchins *et al.* (2009) observed the spatial attenuation, in a ZPG boundary layer, to be negligible for $z^+ > 150$ ($z/\delta > 0.02$). While these numbers cannot be directly extended to a strong APG case, the analysis here concerns only the outer 90 % of the boundary layer, where the spatial attenuation is not expected to be significant. This is supported by the fact that the PIV results (§ 2.4.2) – which could suffer from far greater attenuation due to a significantly

larger interrogation volume – show agreement with hot-wire results to within 7 % (see Appendix A), which is of the order of the uncertainty itself.

Additionally, the three-component velocity was measured with a four-sensor hot-wire probe, with each sensor approximately 0.75 mm long and a measurement volume of 0.5 mm^3, manufactured by Auspex Corporation (type AVOP-4-100). Measurements were made precisely at all the points where the upstream single wire sensor was traversed, enabling cross-validation. The construction, angle and velocity calibration and validation of the probes are discussed by Wittmer, Devenport & Zsoldos (1998). While the mean velocity was generally found to be in agreement with PIV estimates (see Appendix A), results are ignored at all positions with turbulent intensity greater than 20 % (typically in the lower 40 % of the boundary layer) due to significant bias from rectification and axial sensitivity.

The correlation structure of the boundary layer was measured at the BOR tail ($x/D = 3.172$) with two single hot-wires, in the anchored probe – moving probe arrangement, shown in figure 4(*b*,*c*). Radial and circumferential correlations of unsteady streamwise velocity were measured at four anchor points in the boundary layer (40 %, 65 %, 75 %, 85 % of boundary layer thickness from the surface). Furthermore, the radial correlations were consistent with planar PIV results, suggesting negligible probe interference even at small separation.

All hot-wire measurements were made in a horizontal plane (x–z) passing through the BOR axis, away from the tether wake regions, with Dantec 90C10 constant-temperature anemometer modules on a Dantec Streamline 90N10 frame with a flat response up to 10 kHz. The probes were positioned by a computer-controlled three-axis traverse system with a 0.0125 mm resolution. A National Instruments device (NI DAQ 9225-9191) sampled the anemometer output at 50 kHz, obtaining 50 ensembles with 4096 samples in each. Each ensemble was approximately spaced by 1 s, resulting in a total sampling duration of 70 s, ensuring which the statistics are estimated from at least 17 000 boundary layer turnover times (TU_e/δ, where T is the total sampling duration).

2.4.2. *Particle image velocimetry*

Planar PIV measurements were made over the rear 1/3rd of the BOR ramp ($x/D = 2.80$–3.172, see figure 3) to obtain the spatial structure of the turbulence non-intrusively, supplementing the hot-wire measurements. The flow was seeded by a LaVision Aerosol Generator which atomizes di-ethyl-hexyl-sebacat liquid and is expected to produce particles of the order of 1 μm in diameter. The Stokes number for these particles in the low-speed flow is much less than one, even for the smallest scales of interest. A Quantel Evergreen (EVG00200) double-pulsed 532 nm Nd-YAG laser pulsing at 7 Hz, illuminated the seed particles in the horizontal (x–z) plane passing through the BOR axis, shown in figure 5. A LaVision collimator along with a plano-convex lens of −50 mm focal length were used to shape the laser beam into a sheet approximately 1.5 mm thick. The region on the BOR illuminated by the laser was spray painted with Kiton Red 620 dye, which shifts the wavelength of the reflected light, minimizing the laser flare as seen by the camera when fitted with a band-pass filter.

Two LaVision Imager sCMOS cameras (2560 px × 2160 px), each with a Sigma EX 105 mm DG Macro lens (with f2.8), were positioned in tandem outside the flow, at a working distance of 0.92 m, yielding a spatial resolution of 16.2 pixel mm^{-1}. The imaged particle diameter was between 3 and 5 pixels, outside the range of diameters susceptible to peak locking (see Raffel *et al.* 2018) which was verified by examining the histograms

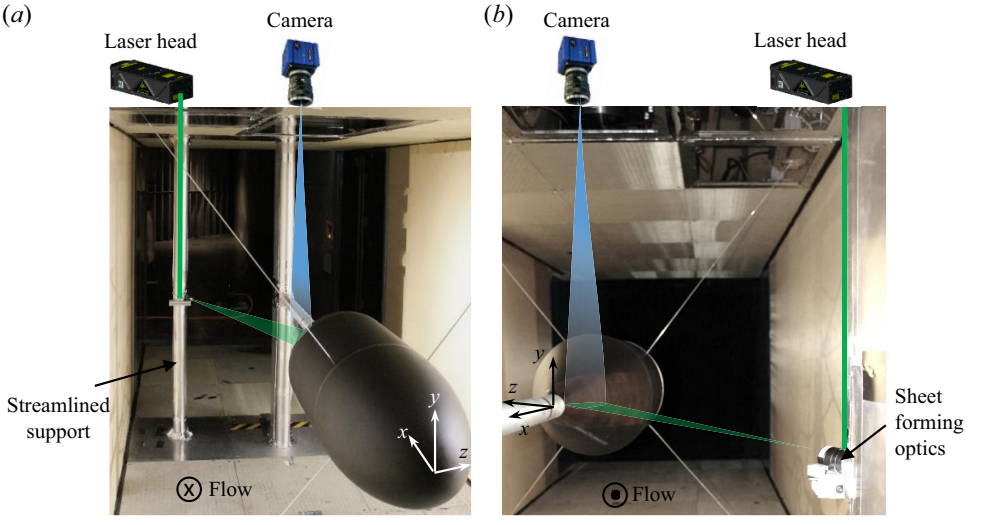

Figure 5. Set-up for PIV measurements on the tail cone. Laser sheet illuminated the tail boundary layer, and a single camera mounted directly above the field of view was traversed along the ramp.

of particle displacement. The camera–lens system, positioned parallel to the measurement plane, was calibrated in DaVis 8.4 using a LaVision Type 31 calibration plate aligned with the BOR tail, to provide velocity components parallel and normal to the BOR surface. A total of 6000 double-frame images were acquired with a time delay of approximately 32 μs between each image pair, yielding a free-stream displacement of between 9 and 11 pixels. The dual cameras provided a combined larger field of view (with a 50 % overlap) and were stitched during post-processing. A total of four such measurement sequences were used to capture the spatial structure of the turbulence over the rear third of the ramp.

The raw images were processed through multiple passes, beginning with a 128×128 pixel interrogation window (with 50 % overlap) and culminating in a 32×32 pixel window (with 75 % overlap), yielding a vector field with a resolution of 0.5 mm. With a 32×32 interrogation window and laser sheet thickness of approximately 1.5 mm, the spatial resolution of the PIV, expressed in wall units ($\Delta x^+ \times \Delta z^+ \times \Delta y^+$), ranged from $55 \times 55 \times 42$ upstream to $30 \times 30 \times 23$ downstream. Comparisons of the mean velocity and turbulence stress with the single hot-wire estimates are shown in Appendix A (figure 28*a–f*) for multiple locations along the ramp. The mean-velocity estimates are consistent with the single hot-wire results (with a spatial resolution of $0 \times 0 \times l^+$ where l^+ varied from 18 to 33) as observed by previous studies examining the spatial averaging in zero pressure gradient boundary layers (Atkinson *et al.* 2013; Lee *et al.* 2016). While these studies observed the Reynolds stress estimates to be attenuated by as much as 50 %, an agreement to within 7 % with the hot-wire results indicates that the spatial averaging does not significantly affect the PIV results in our case.

3. Results and discussion

Results are discussed in the coordinate system (x, y, z) shown earlier in figure 1. The mean velocity along x, y, z axes will be identified by U, V, W, respectively, with U_s implying the velocity in the mean streamwise direction (i.e. velocity magnitude from axial and radial

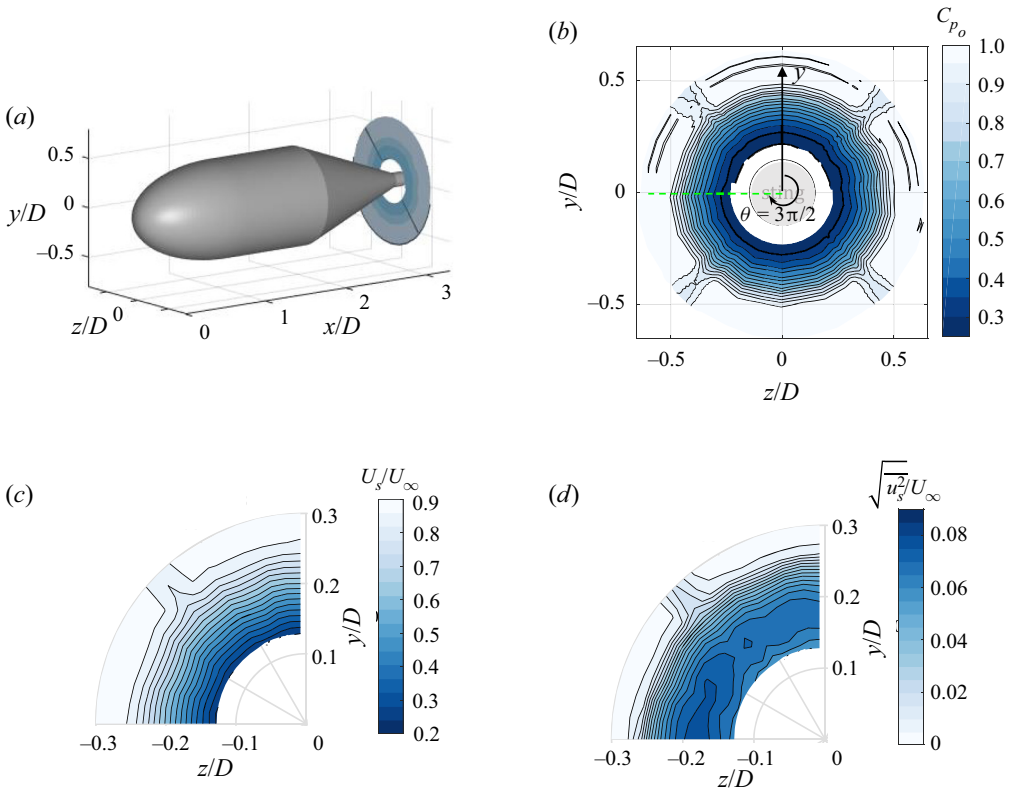

Figure 6. (*a*) Schematic showing the location of stagnation pressure cross-section measured to verify circumferential uniformity. (*b*) Contours of stagnation pressure coefficient (C_{p_o}) at BOR tail verifying circumferential uniformity; green dashed line represents the turbulence measurement plane. (*c*) Contours of streamwise mean velocity over a quadrant at the BOR tail revealing the axisymmetry. (*d*) Contours of streamwise turbulence intensity on a grid similar to that of mean velocity in (*c*).

components excluding the negligible circumferential component). The corresponding unsteady velocities are referred to in the lower case – u, v, w and u_s. The tunnel reference velocity at the test-section inlet is U_∞. In the corresponding cylindrical coordinate system (x, r, θ), r is the radial distance from the x-axis and θ is the polar angle, measured from the vertical (y-axis) by the right-hand rule. By such a convention, all measurements discussed from § 3.3 onwards were made at $\theta = 3\pi/2$. Note that while the velocity statistics as discussed in §§ 3.3–3.7 are measured by traversing the hot-wire radially outward with the velocity resolved in the streamline oriented coordinate system, instead of in the conventional wall-normal traverse, with the velocity in a fixed wall-aligned coordinate system, this does not impact the analysis and conclusions of the work, as demonstrated in Appendix B.

3.1. *Axial symmetry, impact of tethers and trip height*

The axial symmetry of the flow was examined at two axial stations, in different flow quantities; upstream, on the nose ($x/D = 0.5$), mean surface pressure was examined; downstream, at the BOR tail ($x/D = 3.172$) stagnation pressure, mean velocity and turbulence intensity were examined. The circumferential ring of surface pressure taps

on the nose ($x/D = 0.5$) suggested a residual $\pm 0.25^\circ$ angle of attack. Contours of the stagnation pressure coefficient (C_{p_o}) at the BOR tail are shown in figure 6(*a*,*b*). Here, $C_{p_o} = (p_o - p_\infty)/(p_{o,\infty} - p_\infty)$ where p_o is the stagnation pressure in the wake, $p_{o,\infty}$ is the stagnation pressure of the ambient free stream, p_∞ is the static pressure of the tunnel ambient. Outside the wakes from the upstream tethers C_{p_o} is axisymmetric, varying within 9 % from the circumferential average, with a standard deviation of 5 %.

Similarly, uniformity in both the mean velocity and turbulence intensity at the BOR tail (figure 6*c*,*d*) were examined with a single hot-wire, over a 200 point-grid spread across 15 radial profiles covering a quadrant ($+y$, $-z$). The mean velocity was axisymmetric to within 2 % of the circumferential mean, and the turbulence intensity was axisymmetric to within 7 %. Note that the tether wakes shown in figure 6 correspond to the original 1.6 mm tethers which were upgraded to 0.9 mm over the course of the experiments. The wakes of upgraded tethers, measured outside the BOR boundary layer at $x/D = 3.172$, were found to be approximately 10° wide and were mild, with a $0.05U_\infty$ peak velocity deficit, and $0.015U_\infty$ peak turbulence intensity. Additionally, the impact of these tethers on the BOR boundary layer seems constrained, if not negligible, since the boundary layer velocity and turbulent intensity at the BOR tail, directly downstream of the tethers, indicated no explicit variation from the other circumferential stations. Regardless, all turbulence measurements, discussed in subsequent sections were made at the plane furthest away from the tethers ($\theta = 3\pi/2$ see figure 6*b*).

The sensitivity of the flow to trip height was examined, by replacing the original 0.8 mm one with a trip double the height, and comparing the stagnation pressure profiles at the BOR tail. The resultant wake was slightly stronger, with roughly 9 % lower C_{p_o}, suggesting the turbulence structure is not overly sensitive to the trip.

3.2. *Characteristics of the inflow to the APG ramp*

The streamwise variation of mean pressure along the body is shown in figure 7. Estimates of the static-pressure coefficient (C_p) are consistent with potential flow calculations (using a doublet panel method for a BOR) and in turn with numerical simulations (wall-modelled large eddy simulation) from Zhou, Wang & Wang (2020). The flow accelerates over the nose, passing the trip ring sandwiched between the nose and the constant diameter mid-body. Further downstream, the sharp corner between the mid-body and ramp generates an intense local acceleration as the flow enters the ramp. Hereafter, the flow decelerates rapidly over the 20° tail cone, with the boundary layer resisting a strong APG.

The boundary layer approaching the ramp has been documented to understand the initial conditions for the APG region. The mean velocity and turbulence intensity approximately 10 mm upstream of the corner ($x/D = 1.977$), sampled by a single hot-wire, are shown in figure 8(*a*,*b*). Here, the vertical axis represents the position (z) relative to the surface (z_s), scaled on the BOR diameter, while the horizontal axis reveals the corresponding mean velocity (figure 8*a*) and turbulence intensity (figure 8*b*). Generally, the mean velocity (U_s) is higher compared with the tunnel inlet velocity due to the acceleration past the nose, and does not fully asymptote to a constant due to the local acceleration and curvature induced by the downstream corner. The boundary layer thickness – defined throughout this paper as the location from the surface with a turbulence intensity of 2 % – is 8.4 mm, and is thin relative to the local radius ($\delta/r_s = 0.04$). The peak measured turbulence intensity is approximately 9 %, occurring at 0.12δ from the surface, and decays on moving further away. Additional characteristics of the layer such as the integral parameters are shown in table 1. The displacement and momentum thicknesses, δ_1 and δ_2, respectively, have been

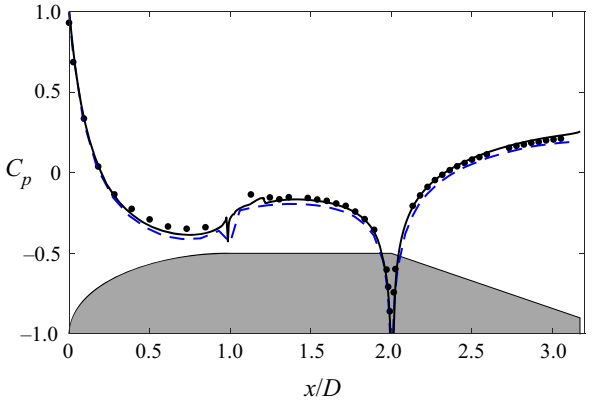

Figure 7. Streamwise pressure distribution on the BOR; (black circle) measurement, (blue dash line) potential flow simulation, (black line) large eddy simulation (LES) from Zhou *et al.* (2020).

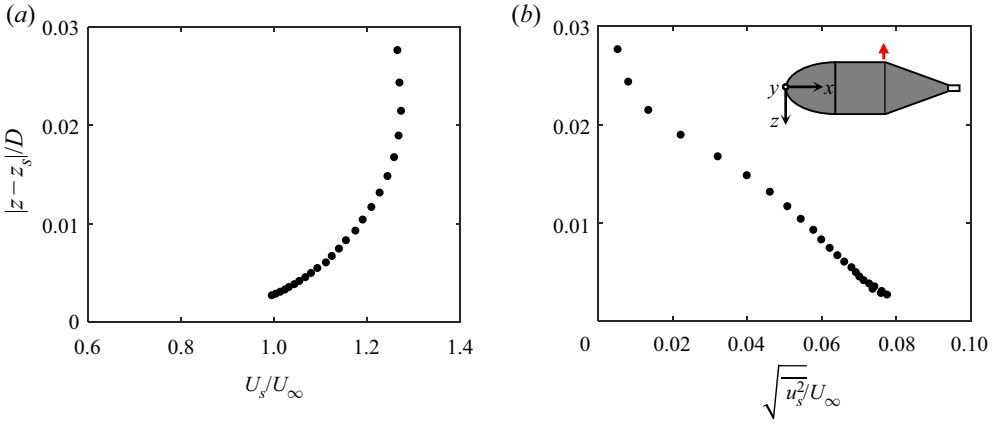

Figure 8. (*a*) Mean-velocity profile upstream of corner ($x/D = 1.977$), U_∞ is the tunnel free-stream velocity (see table 1). (*b*) Turbulence intensity profile at $x/D = 1.977$.

estimated using the planar definitions (3.1), where the missing data very near the wall have been extrapolated by a cubic spline fit, constrained by a no-slip condition at the wall. The results were only mildly sensitive to the extrapolation process, varying within 5 % of the spline estimates, when tried with linear, cubic, and quadratic extrapolations.

$$\left.\begin{aligned} \delta_1 &= \int_0^\delta (1 - U_s/U_e)\,\mathrm{d}(|z - z_s|), \\ \delta_2 &= \int_0^\delta (U_s/U_e)(1 - U_s/U_e)\,\mathrm{d}(|z - z_s|). \end{aligned}\right\} \tag{3.1}$$

3.3. *Mean flow characteristics on the ramp*

Downstream of the corner, the mean flow decelerates significantly on the ramp with the boundary layer thickening, as seen from the streamwise mean-velocity contours in figure 9. At the BOR tail ($x/D = 3.172$) the boundary layer is 79.5 mm thick; growing approximately 10 times the thickness just upstream of the corner, over a distance of $1.2D$.

Tunnel inlet velocity	Edge velocity	Boundary layer thickness	Displacement thickness	Shape factor	Reynolds number	Curvature parameter
U_∞ (ms^{-1})	U_e/U_∞	δ (mm)	δ_1 (mm)	δ_1/δ_2	Re_{δ_2}	δ/r_s
22.8	1.27	8.4	1.0	1.53	1530	0.04

Table 1. Boundary layer characteristics at inflow ($x/D = 1.977$) to the BOR ramp.

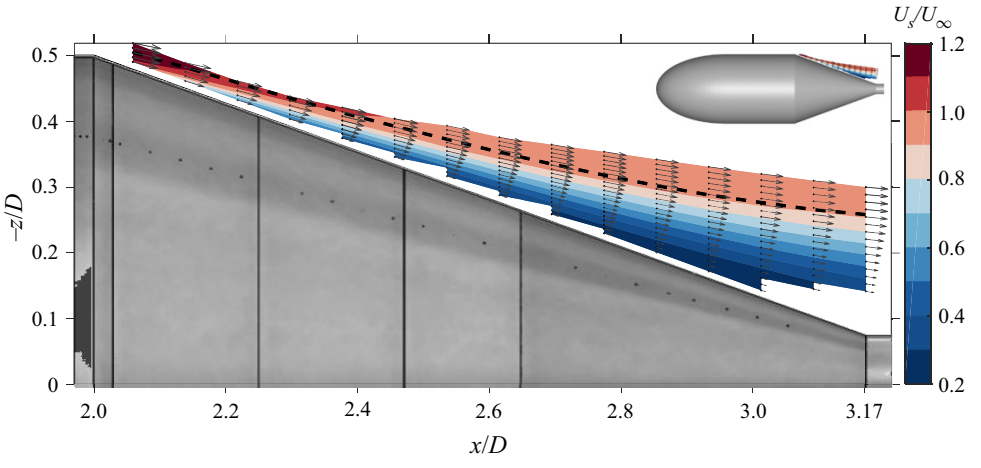

Figure 9. Contours of streamwise mean velocity (U_s) on the ramp from single hot-wire measurements, scaled on the tunnel reference velocity (U_∞). Arrows at the measurement stations reveal the flow orientation as measured by quadwire; black dashed line identifies the edge of the boundary layer. Inset to the top right shows the global position of the measurement.

The corresponding velocity at the edge of the boundary layer (U_e) decreases by over 40 %, from $1.27U_\infty$ upstream to $0.89U_\infty$ at the tail. Despite such a strong deceleration, the flow is well behaved, as seen from the velocity vectors in figure 9, diverging away from the wall and increasingly aligned with the BOR axis. The circumferential velocity measured by a quadwire, reliable only in the outer 60 %, was less than 8 % U_s. While the inner 40 % of the boundary layer saw a stronger circumferential component that varied along the tail, it is strongly corrupted by significant bias errors due to the highly turbulent flow probed with a sensor not aligned with the streamwise direction. However, auxiliary measurements discussed in § 3.1 suggest that it is unlikely that the flow is significantly three-dimensional.

The flow appears to be out of equilibrium, as seen from the downstream evolution of boundary layer characteristics, shown partially in figure 10(*a–c*) with full details in table 2. Note that all integral parameters have been estimated by integrating radially outward (due to the orientation of the profiles) instead of normal to the surface; however, it was found that the resulting parameters are consistent to within 5 % of their counterparts estimated in the conventional boundary layer coordinates (see Appendix B). The displacement thickness, shown in figure 10(*a*), (estimated according to (3.1)), increases relative to the boundary layer thickness from 0.2δ to 0.5δ, suggesting a stronger wake component downstream and the corresponding shape factor H ($= \delta_1/\delta_2$), shown in figure 10(*b*), increases by over 50 %, from 2.14 upstream to 3.24 at the tail. The associated momentum thickness based Reynolds number Re_{δ_2} (table 2) rises by an order of magnitude,

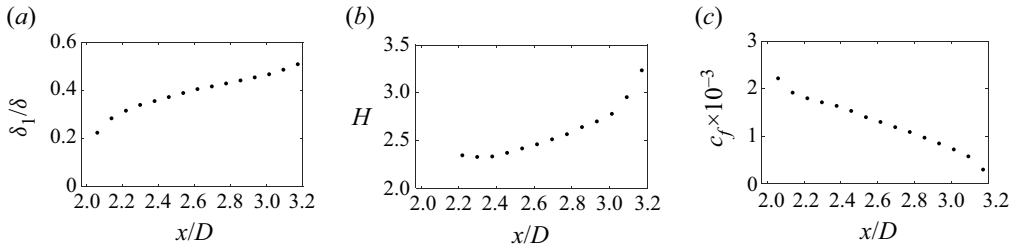

Figure 10. Characteristics of boundary layer on ramp: (*a*) displacement thickness (δ_1) as a fraction of the velocity thickness (δ), (*b*) shape factor $H = \delta_1/\delta_2$, (*c*) skin-friction coefficient (C_f) from LES (Zhou *et al.* 2020).

from some 2000 upstream to approximately 16 000 at the ramp tail. While the shear stress at the wall was not measured, and since no universally accepted hypothesis exists to empirically estimate the value, we infer the trends in wall friction from Reynolds number matched LES of the BOR flow, borrowed from Zhou *et al.* (2020). Even after confirming the agreement in the mean surface pressure (figure 7), in the mean velocity as well as auto-spectra of unsteady surface pressure (refer to Zhou *et al.* 2020), we rely on the estimates only for qualitative conclusions: here, that the skin friction is not constant across the ramp (figure 10*c*). Therefore, a strongly varying H, Re_{δ_2} and C_f suggests the non-equilibrium character of the flow.

The strength of the pressure gradient has been previously inferred from various parameters, with the most common being Clauser's $\beta_C = (\delta_1/\tau_w)\,\mathrm{d}p/\mathrm{d}x$ (Clauser 1954), where τ_w is the shear stress at the wall; in our case, β_C (table 2) varies between 5 and 18, except at the tail ($\beta_C = -14.7$) due to the flow accelerating onto the support shaft (see figure 1). However, β_C is not universally applicable, as it tends to infinity for separating boundary layers ($\tau_w \to 0$). More importantly, Maciel *et al.* (2018) argued that β_C and Re_{δ_2} do not form a consistent set of parameters that describe the flow; specifically, these parameters have not been derived from the boundary layer equations using a consistent choice of length and velocity scales. As a remedy to this problem, they developed a set of parameters from the non-dimensional boundary layer equations, using a consistent choice of length and velocity scales, say L_o and U_o. The resulting parameters: $\beta_o = L_o/(\rho U_o^2)\,\mathrm{d}p_e/\mathrm{d}x$, $\alpha_o = U_e V_e/U_o^2$ and $Re_o = U_o L_o/\nu(U_o/U_e)$ were found to have a direct physical interpretation: they represented the ratio of the order of magnitude of the forces, with the apparent turbulent force (Reynolds shear-stress gradient) as the reference force; β_o, α_o and Re_o, represented the strength of the pressure gradient force, inertial and viscous forces, respectively, relative to the apparent turbulence force. Furthermore, on examining their DNS datasets, they observed that these parameters, with velocity scale $U_o = U_{zs} = U_e\delta_1/\delta$ and length scale $L_o = \delta$, accurately tracked the ratio of the forces. Here, U_{zs} represents the velocity defect of the bulk flow, first proposed by Zagarola & Smits (1998) for the pipe flows, and later examined for APG layers first by Castillo & George (2001). The parameters β_{zs} and Re_{zs} on the BOR ramp, based on the characteristics in table 2, are shown in figure 11(*a*,*b*). For reference, β_{zs} is co-presented with Castillo's pressure gradient parameter, $\Lambda = (\delta/(U_e\,\mathrm{d}\delta/\mathrm{d}x))\,\mathrm{d}U_e/\mathrm{d}x$ in figure 11(*a*), while Re_{zs} is shown with Re_{δ_2} in figure 11(*b*). Three observations can be made; first, the flow is confirmed to be out of dynamic equilibrium since the parameters, representing the ratios of the fluid forces, vary strongly across the ramp; second, the pressure gradient is strong relative to the turbulent force ((pressure gradient)/(turbulent force) $\approx 10\beta_{ZS}$) and decays downstream on the tail; third, the turbulent force is stronger than the viscous force,

https://doi.org/10.1017/jfm.2021.845 Published online by Cambridge University Press

x/D	U_∞ (ms^{-1})	U_e/U_∞	δ (m)	δ_1 (m)	$H (= \delta_1/\delta_2)$	Re_{δ_2}	U_τ/U_∞	C_f	β_C	δ/r_s	r_s^+	l^+
2.059	24.5	1.22	0.0114	0.0025	2.14	1981	0.0405	0.0022	5.0	0.06	11 458	67
2.138	24.6	1.12	0.0140	0.0040	2.38	2593	0.0347	0.0019	7.7	0.07	9291	57
2.218	24.6	1.07	0.0164	0.0052	2.35	3260	0.0320	0.0018	7.2	0.09	8025	53
2.297	24.6	1.03	0.0189	0.0064	2.33	3927	0.0301	0.0017	7.3	0.11	7048	50
2.377	24.6	1.00	0.0217	0.0077	2.33	4597	0.0286	0.0016	11.2	0.14	6222	48
2.456	23.7	0.98	0.0254	0.0094	2.37	5325	0.0272	0.0015	14.7	0.18	5332	44
2.536	23.2	0.98	0.0293	0.0114	2.42	6280	0.0259	0.0014	12.5	0.22	4635	42
2.615	23.0	0.96	0.0333	0.0135	2.46	7190	0.0245	0.0013	13.2	0.28	3976	40
2.695	22.8	0.95	0.0380	0.0158	2.51	8133	0.0231	0.0012	17.3	0.36	3357	38
2.774	22.7	0.93	0.0432	0.0186	2.57	9191	0.0218	0.0011	18.4	0.46	2791	36
2.854	22.6	0.92	0.0488	0.0216	2.64	10298	0.0203	0.0010	15.2	0.60	2266	33
2.933	22.5	0.92	0.0552	0.0251	2.70	11638	0.0189	0.0008	14.2	0.80	1782	31
3.013	22.5	0.91	0.0627	0.0293	2.78	13175	0.0173	0.0007	15.6	1.11	1344	28
3.092	22.4	0.91	0.0706	0.0343	2.95	14434	0.0154	0.0006	11.7	1.60	929	25
3.172	22.4	0.91	0.0798	0.0406	3.24	15661	0.0110	0.0003	−14.7	2.51	477	18

Table 2. Boundary layer characteristics on the ramp. Here, C_f, U_τ are obtained from large eddy simulations on the BOR at matched Reynolds number (Zhou *et al.* 2020).

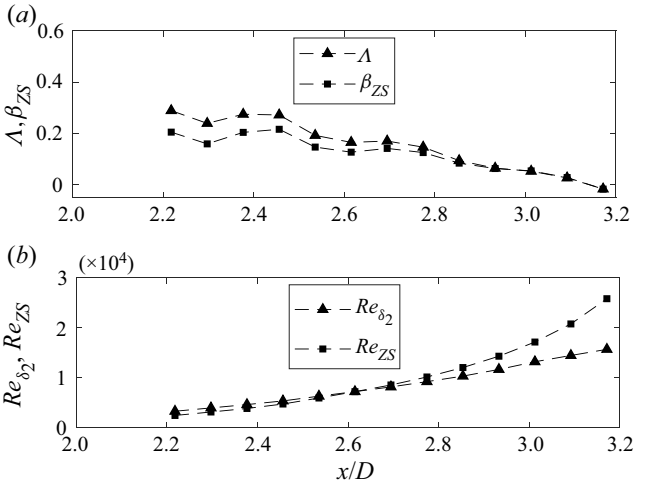

Figure 11. Flow parameters in APG region. (*a*) Pressure gradient parameters, $\Lambda = (\delta/(U_e\,\mathrm{d}\delta/\mathrm{d}x))\,\mathrm{d}U_e/\mathrm{d}x$ and $\beta_{ZS} = (\delta/U^2{}_{zs})U_e\,\mathrm{d}U_e/\mathrm{d}x$ following the work of Castillo & George (2001) and Maciel *et al.* (2018), respectively. (*b*) Reynolds numbers, $Re_{\delta_2} = \delta_2 U_e/\nu$, and $Re_{zs} = U_{zs}\delta/\nu(U_{zs}/U_e)$.

even more so downstream, implying that the pressure gradient dominates both the turbulent and therefore the viscous forces.

While this non-equilibrium boundary layer over the ramp suffers a strong APG, the effect of transverse curvature appears to be mild. The curvature parameter, δ/r_s is mostly less than 1 (table 2), implying the boundary layer is thinner than the local radius of curvature (r_s) except near the BOR tail. The radius based Reynolds number, $r_s^+ = r_s u_\tau/\nu$, although initially high at approximately 11 000, decreases to 477 at the BOR tail. Following the observations of Piquet & Patel (1999) and Snarski & Lueptow (1995) such a range of parameters may affect the mean flow and turbulence statistics moderately, but is not expected to strongly influence the fundamental turbulence mechanisms. The flow, therefore, corresponds to that of a high Reynolds number, strongly decelerating flow over a large cylinder, subjected to an axially varying lateral curvature and pressure gradient.

3.4. *Turbulence statistics on the APG ramp*

The streamwise evolution of Reynolds normal stress ($\overline{u_s^2}/U_\infty^2$), measured with a single hot-wire, is contoured in figure 12. Consistent with previous studies, $\overline{u_s^2}$ develop an 'outer' peak as the flow decelerates, which is centred initially about 0.4δ from the surface, drifting further away downstream and reaching $\sim 0.55\delta$ at the tail. However, contrary to most studies on planar APG boundary layers where the peak intensified with the pressure gradient, we observe the peak to relax downstream, even if normalized by the edge velocity (U_e). This can be viewed as a response to transverse curvature combined with a decreasing local pressure gradient (see figure 11*a*). In an LES study of a BOR flow, Kumar & Mahesh (2018*a*) observed the turbulence intensity away from the wall to decay faster than in a flat-plate flow under similar conditions, even for a modest δ/r_s of 0.3. This is also consistent with earlier work by Piquet & Patel (1999), who showed that the transverse curvature does not alter the turbulence production mechanism itself, but the reduction of turbulence activity compared with a planar boundary layer is merely due to a smaller surface area where the production occurs, and the corresponding vorticity per unit volume

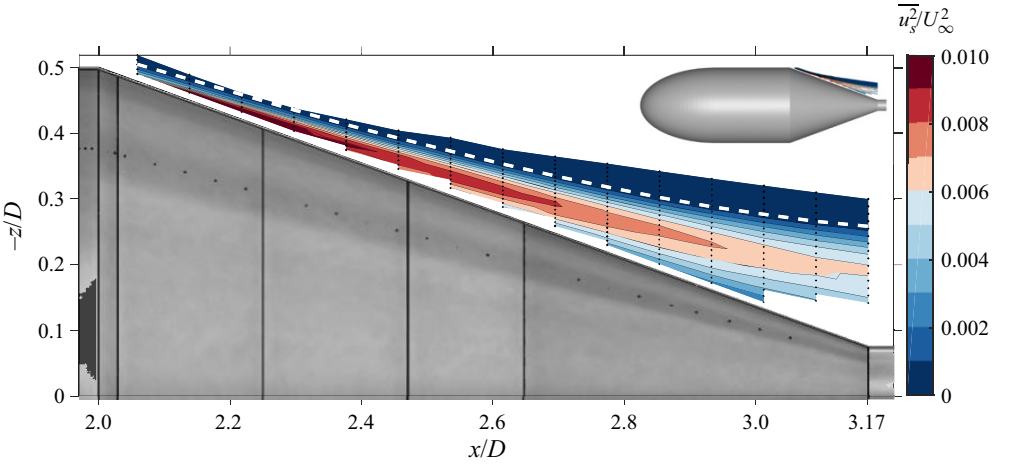

Figure 12. Contours of streamwise Reynolds normal stress on the ramp from single hot-wire measurements, scaled on the tunnel reference velocity. White dashed line indicates the boundary layer edge. Inset to the top right shows the global position of the measurement.

of the flow, introduced by this surface, is lower than in the planar boundary layer. However, if the stress profiles are scaled with the friction velocity, the expected trend of a magnifying peak is observed, suggesting that the turbulent motions responsible for the outer peak are not dictated by the near-wall shear-stress inducing motions.

The structure of the other in-plane Reynolds stresses, u_n^2 (resolved orthogonal to the streamline) and $u_s u_n$, is similar to that of the streamwise Reynolds stress discussed above. In fact, this is not just superficially true, since the various Reynolds stresses were found to be directly proportional to the in-plane turbulent kinetic energy (TKE), $E = 0.5(\overline{u_s^2} + \overline{u_n^2})$ through precise constants over the measured domain, as shown in figure 13. While the contours of E in figure 13(a) – obtained from planar PIV over the rear third of the ramp – paint a picture consistent with the hot-wire estimates of $\overline{u_s^2}$ stress in figure 12, the ratios of $\overline{u_s^2}$, $\overline{u_n^2}$ and $\overline{u_s u_n}$ to E, shown in figure 13(b–d), are invariant over the measured domain; $\overline{u_s^2}$ and $\overline{u_n^2}$ are consistently approximately $1.4E$ and $0.6E$, and the Reynolds shear stress $u_s u_n$ is invariant at $-0.45E$. This behaviour deviates only near the boundary layer edge, as seen about the white dashed line in figure 13(b,c), where $\overline{u_n^2}$ dominates, as one might expect due to the oscillating turbulent–non-turbulent interface. In any case, apart from being a pleasant simplification in extracting the different components from just the TKE through simple RANS calculations, this is an interesting observation. While we do not have a definite explanation, there appears to be some sort of self-preserved structure of the turbulent motions, with a dominant, organized mode through which the streamwise turbulent energy is transferred into the other components. As a first step towards understanding this, we examine the mean flow and turbulence statistics for self-similarity in the following section, deriving the associated length and velocity scales, which will be further examined on the turbulence and correlation structure in subsequent sections.

3.5. *Self-similarity in the outer region along the ramp*

Figure 14(a,b) shows the profiles of streamwise velocity and Reynolds normal stress, obtained from a single hot-wire, that correspond to the contours in figures 9 and 12

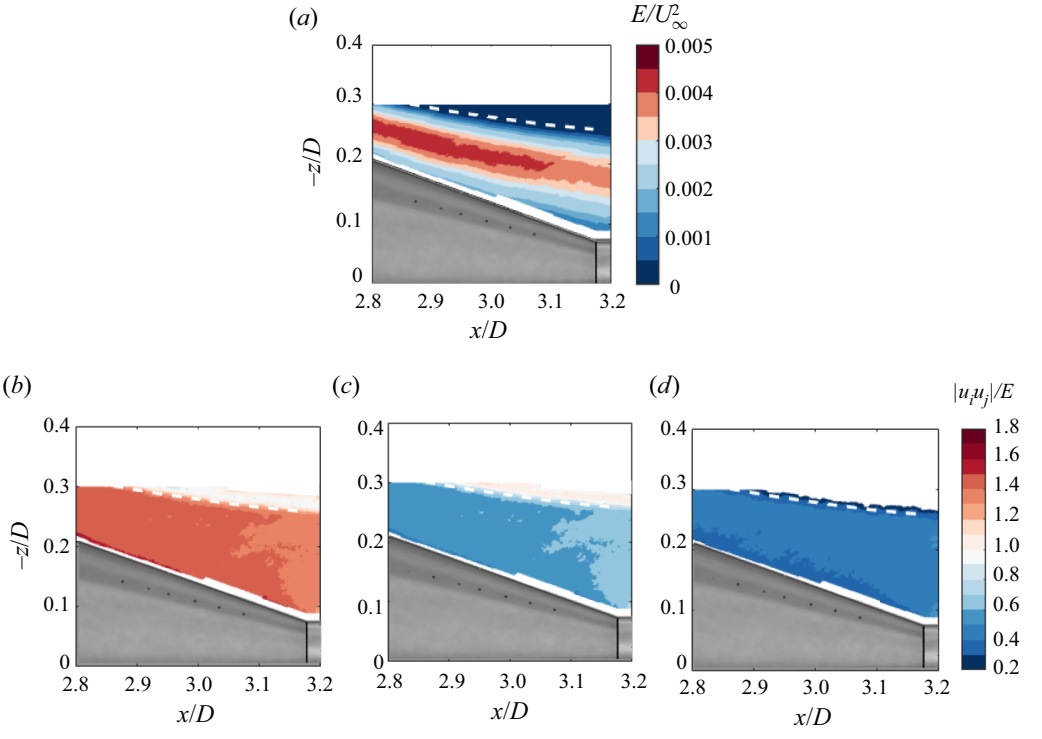

Figure 13. (*a*) Turbulence kinetic energy based on in-plane Reynolds normal stresses ($E/U_\infty^2 = 0.5(\overline{u_s^2} + \overline{u_n^2})/U_\infty^2$) from PIV; (*b*) ratio of streamwise normal stress to kinetic energy ($\overline{u_s^2}/E \approx 1.4$; (*c*) $\overline{u_n^2}/E \approx 0.6$; (*d*) $\overline{u_s u_n}/E \approx 0.45$.

discussed earlier. While the position from the wall is scaled with the boundary layer thickness, the mean velocity, figure 14(*a*), and turbulence stress, figure 14(*b*), are scaled with the edge velocity $U_e(x)$. Supporting the preliminary observations in §§ 3.3 and 3.4, the character of the profile changes significantly as the flow decelerates downstream. The velocity deficit increases across the boundary layer and the outer peak in the Reynolds stress weakens as it drifts higher in the boundary layer, reaching 0.55δ at the tail. Much of this streamwise variation can be accounted for, when δ is replaced by δ_1 as the length scale, as shown in figure 15(*a*,*b*). In general, the mean-velocity profiles form a tighter collapse while the Reynolds stress profiles realign such that the functional form, especially near the peak, is somewhat consistent. Furthermore, the position of the outer peak is almost invariant at $(1.2 \pm 0.06)\delta_1$ (figure 15*c*) and we find that the mean-velocity profiles exhibit an inflection point at this position. This is consistent with Kitsios *et al.*'s (2017) observation of an inflection point collocated with the outer turbulence peak, occurring at $1.3\delta_1$ and $1\delta_1$ for their mild ($\beta_C = 1$) and strong ($\beta_C = 39$) pressure gradient cases. Further confirming this, Maciel *et al.* (2018) observed the peak in the range 1.0–$1.3\delta_1$ for a diverse range of numerical and experimental datasets of non-equilibrium layers. While the relationship between the outer turbulence peak and δ_1 is worth exploring, the success of the $U_e - \delta_1$ scaling is limited only to the vicinity of the Reynolds stress peaks, as evident from the spread in the profiles at positions further away. On that note, by examining several scalings in the literature Maciel *et al.* argued that it is impossible to produce a complete collapse of the profiles, especially of the second-order statistics, and suggested

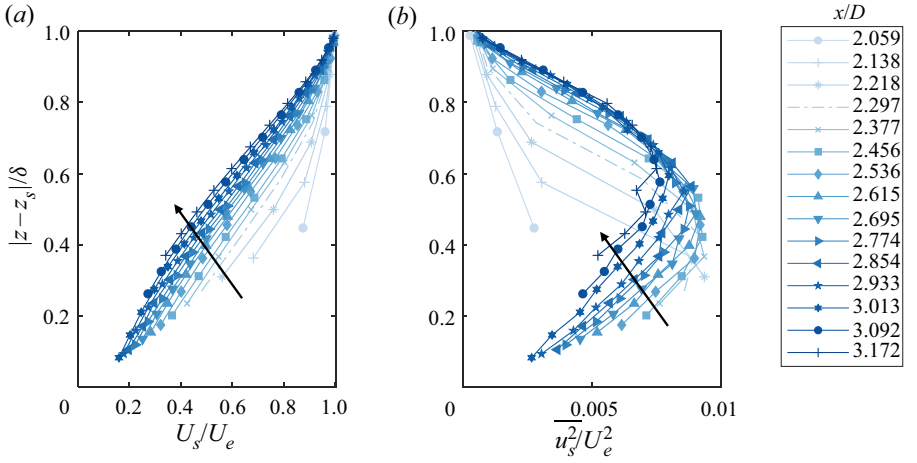

Figure 14. (*a*) Mean-velocity profiles, with the vertical axis representing the distance from the surface scaled with δ and the horizontal axis representing the velocity scaled with the edge velocity. Black line indicates change in the profiles along the ramp. (*b*) Profiles of the streamwise Reynolds stress with the $U_e - \delta$ scaling. Legend to the right shows the streamwise positions.

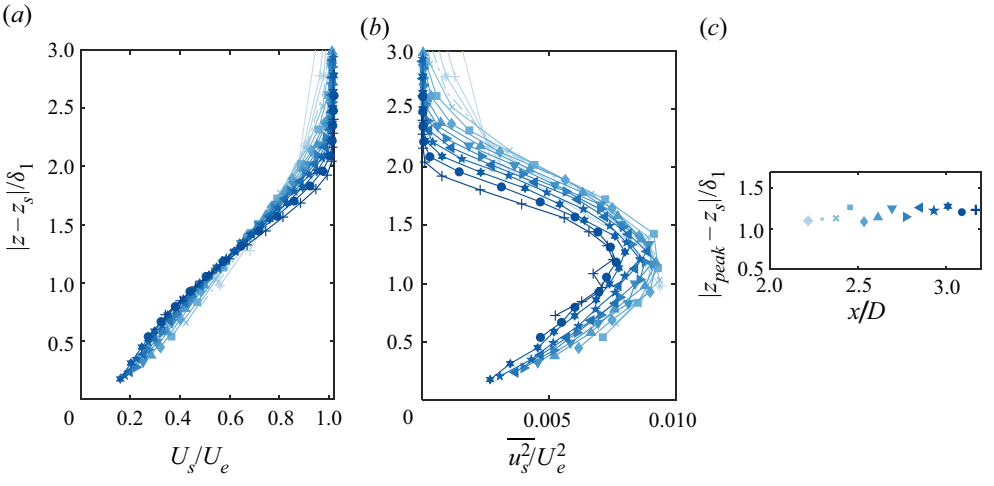

Figure 15. (*a*) Mean-velocity profiles with U_e and δ_1 scaling. (*b*) Profiles of the streamwise Reynolds stress with the U_e and δ_1 scaling. (*c*) Location of the peak streamwise Reynolds stress scaled on δ_1. See figure 14 for legend.

the success of a scaling, over a broad range of APG, can only be judged by the order of magnitude of the resulting collapse. With such a view, they found $U_{zs} = U_e\delta_1/\delta$ and δ was the most successful scaling. Commonly referred to as the Zagarola–Smits scale, this scaling was originally proposed as an outer velocity scale for turbulent pipe flow by Zagarola & Smits (1998) and represents the bulk velocity defect of the flow. While Zagarola–Smits scaling may well be successful when considering a wide range of pressure gradients, for our relatively narrow spectrum of strong APG flow, the performance of $U_{zs} - \delta$ scaling is inferior to both $U_e - \delta_1$ and $U_e - \delta$ scalings. In any case, focusing on the larger picture, where we observe inflectional velocity profiles collocated with turbulence

stress peak in the outer region, combined with a new peak in the turbulence production and transfer observed in other studies (Skåre & Krogstad 1994; Kitsios *et al.* 2017), suggests a fundamentally different mechanism for boundary layers under strong APG.

A promising proposal is that strong APG layers behave more like a free-shear layer, developing inviscid instabilities in the outer regions, while the importance of near-wall turbulence weakens. For example, experimental studies by Elsberry *et al.* (2000), Song *et al.* (2000) and Schatzman & Thomas (2017) as well as a numerical study by Kitsios *et al.* (2017) invoked the similarity with mixing layers. Through detailed investigation, Schatzman & Thomas gathered evidence for coherent spanwise vorticity, centred about the inflection point. Via quadrant analysis of the shear-stress profiles, they observed that the sweeping motions were more frequent above the inflection point, while ejections dominated below. At the inflection point both the motions were equally likely. Invoking the Rayleigh–Fjørtoft theorem they attributed this observation to inviscid instabilities, and hypothesized an 'embedded shear layer' (ESL) in the boundary layer, centred about the inflection point. Inspired from self-similarity in free-shear layers, they proposed the ESL scaling, with the length scale as the vorticity thickness

$$\delta_\omega = (U_e - U_{IP})/(\mathrm{d}U/\mathrm{d}z)_{IP}, \tag{3.2}$$

where IP refers to the outer inflection point and $(\mathrm{d}U/\mathrm{d}z)_{IP}$ is the slope of the velocity profile at the inflection point. The associated velocity scale is the velocity defect at the inflection point

$$U_d = U_e - U_{IP}, \tag{3.3}$$

with these length and velocity scales, and a coordinate system centred about the inflection point (3.4), they observed the mean velocity and Reynolds normal and shear stress to collapse, despite not being in equilibrium

$$\eta = (z - z_{IP})/\delta_\omega, \tag{3.4}$$

$$U^* = (U_e - U)/U_d. \tag{3.5}$$

For our case, the mean-velocity and turbulence stress profiles with the ESL scaling are shown in figure 16(*a*,*b*). In order to minimize the numerical errors related to finding the inflection point, we centred the coordinate system about the location of peak $\overline{u_s^2}$. The velocity defect profiles, figure 16(*a*), collapse well, and the functional form away from the wall ($\eta > -1$) is accurately described by the complementary error function $(1 - \mathrm{erf}(\eta))$, similar to the error function (erf()) commonly used for planar mixing layers (Pope 2001). But, the collapse in the turbulence stress profiles, figure 16(*b*), appears no better than the $U_e - \delta_1$ scaling, particularly on the low-speed side ($\eta < 0$, figure 15*b*). However, a lack of any immediately obvious trend in the spread suggests significant uncertainty, arising from the discretized profiles used to estimate the scaling parameters. Despite a considerable spread, the peak magnitude of the turbulence intensity $\sqrt{\overline{u_s^2}}$ varied between $(0.232 \pm 0.014)U_d$, close to the $0.21U_d$ observed by Schatzman & Thomas. Furthermore, although not shown here, the collapse in the corresponding PIV profiles from the rear third of the ramp was closer to $0.21U_d$.

Examining the shear layer parameters, we observe the vorticity thickness δ_ω to grow almost linearly along the ramp (figure 16*c*), at a rate $\mathrm{d}\delta_\omega/\mathrm{d}x \approx 0.048$, within the range commonly observed in free-shear layer studies (such as Oster & Wygnanski 1982). Furthermore, consistent with the condition for similarity, we observe that the ESL length

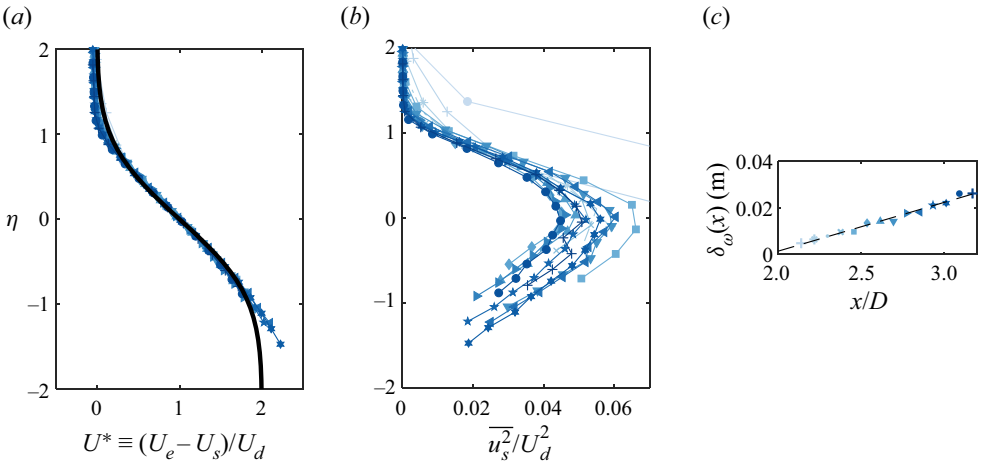

Figure 16. ESL scaling for mean flow. (*a*) Mean-velocity defect profiles, with (black line) representing the complementary error function, $1 - \mathrm{erf}(\eta)$. (*b*) Streamwise Reynolds normal stress profiles. (*c*) Streamwise growth of vorticity thickness (δ_ω) of the shear layer. Slope of the dashed line corresponds to $\mathrm{d}\delta_\omega/\mathrm{d}x \approx 0.048$. For legend, refer figure 14.

and velocity scales are proportional to the boundary layer thickness and edge velocity respectively as

$$\delta_\omega/\delta \approx U_d/U_e \approx 0.4 \pm 0.05. \tag{3.6}$$

Figure 17 shows comparisons of the BOR results with the axisymmetric APG boundary layer measurements of Dengel & Fernholz (1990) (red, hereafter known as DF90), in addition to the planar APG flow DNS of Maciel *et al.* (2018) (black dashed lines, hereafter known as MTGS18). The shape factors for each of the cases – $H = 2.35$ for DF90, and $H = 1.76$–2.94 for MTGS18 (see caption) – are within the range observed on the BOR tail. Since a quantitative survey requires a rigorous study with matched flow parameters, which are yet to be established for APG flows, our intention here is to reveal only qualitative but insightful comparisons. For example, DF90 had a significantly different experimental set-up, with a constant-radius circular cylinder where the APG was enforced through flow suction from porous wind-tunnel walls, unlike a conical contraction for the BOR: the success of the ESL scaling suggests its generic applicability for axisymmetric flows. Similarly, comparisons with the planar and strong APG results of MTGS18 suggest that the flow physics of strong APG boundary layers are not very sensitive to the flow history or specific boundary conditions. As a side note, the ESL scaled turbulence intensity profiles have a wider spread, especially near the peak and in the low-speed regions ($\eta < 0$), suggesting that the peak value of $0.21U_d$ reported by Schatzman & Thomas (2017) is not strictly universal.

While these observations certainly advocate the success of ESL scaling for axisymmetric APG boundary layers, some fundamental questions remain open. The idea that the instantaneous flow can 'see' the mean-velocity profile, and therefore the inviscid instabilities from inflection points is debatable. Previous studies in fully turbulent free-shear flows (see Wygnanski, Champagne & Marasli 1986) have observed that the linear stability analysis of inflectional mean-velocity profiles yielded eigen-solutions that resemble the turbulent intensity profiles. Extending the analysis to wall-bounded flows, Michalke (1991) made similar observations for flows approaching separation,

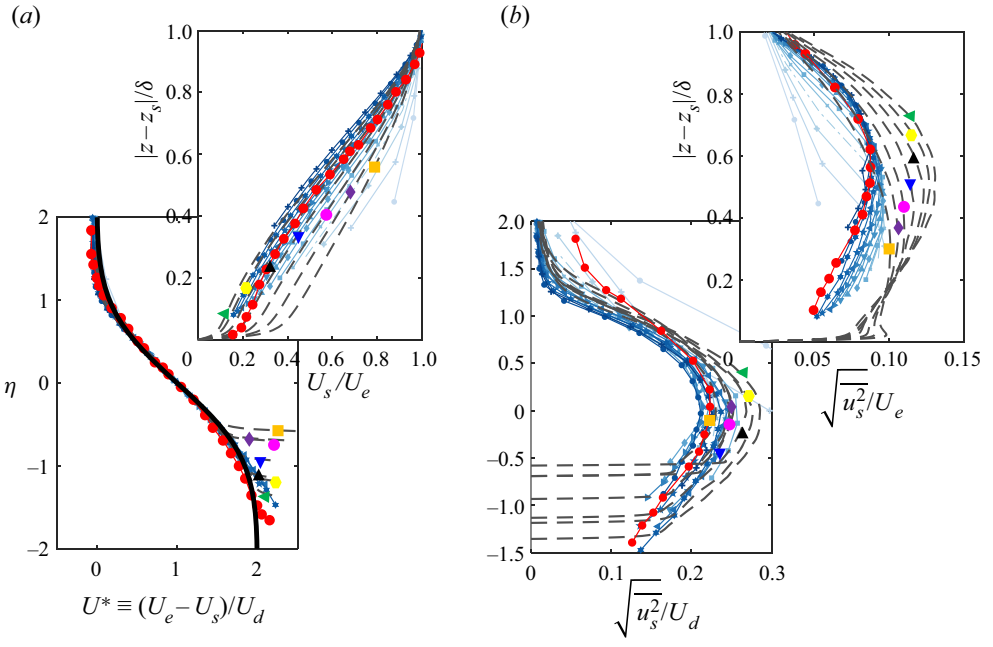

Figure 17. Comparison of BOR profiles (from figures 14 and 16) with previous studies from flat-plate and axisymmetric APG boundary layers. (*a*) ESL scaling for mean velocity; left bottom shows the ESL scaling and right top shows the same data re-plotted with U_e and δ scaling. (*b*) Corresponding turbulence intensity profiles; bottom left shows the comparisons in ESL scaling and top right shows the profiles in U_e and δ scaling. Legend: (redline-redcircle-redline) axisymmetric case, with $H = 2.35$ and $\delta/r_s = 0.2$ (from Dengel & Fernholz (1990), see case 2: $x = 1.131$ m). Black dashed lines correspond to flat-plate results from the DNS2017 case of Maciel *et al.* (2018); (orange square) $H = 1.76$, (purple diamond) $H = 1.92$, (magenta circle) $H = 2.11$, (blue triangledown) $H = 2.34$, (black triangleup) $H = 2.57$, (yellow hexagon) $H = 2.78$, (green triangleleft) $H = 2.94$.

noting that the wall has a stabilizing effect. It certainly seems to be convincing that the inviscid instabilities play an important role. However, Maciel *et al.* (2017) were unable to deduce any coherent structures relevant to inviscid instability, in their sharply decelerated boundary layer. Furthermore, the commonly observed outer stress peak, even for milder APG boundary layers without inflectional profiles, cannot be explained by the instability mechanism. One may therefore speculate that the inflectional velocity profiles and the amplified turbulence activity in the outer regions are just correlated without sharing a cause–effect relationship. Of course, further investigation into this aspect is needed before the scaling can be concretely attributed to inviscid instabilities. Subsequently, some work is also needed to develop a rigorous framework for strong APG layers. We must establish the conditions under which the ESL scaling is valid, and how this ties into the layer structure of the boundary layer, including the near-wall layer.

While the questions raised above must certainly be addressed to illuminate the fundamental physics and develop a rigorous framework for strong APG layers, we are interested in examining the turbulence structure and the implications of the shear layer scaling for the length and time scales of the turbulence. This is expected to provide significant input for the aeroacoustic predictions where the integral length scales and the turbulence quantities are a direct input to the estimate the far-field spectrum, for example when a fan is ingesting the boundary layer.

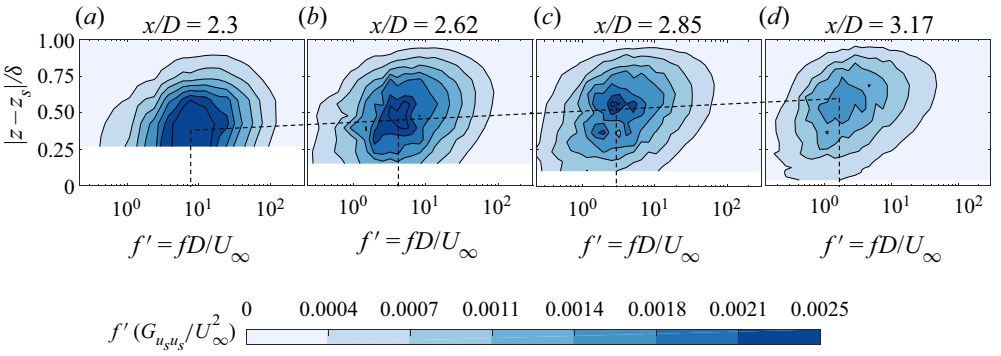

Figure 18. Contours of the pre-multiplied spectra of the streamwise velocity, $f'G_{u_s u_s}/U_\infty^2$, at representative streamwise stations on the ramp. Frequency $f' = fD/U_\infty$, where D is body diameter ($D = 0.4318$ m) and U_∞ is tunnel free-stream velocity; (*a*) $x/D = 2.297$, (*b*), $x/D = 2.615$, (*c*) $x/D = 2.854$, (*d*) $x/D = 3.172$. Dashed lines indicate the position of the peak levels, relative to the surface, and the corresponding frequency.

3.6. *Turbulence structure of streamwise velocity*

The spectral structure of streamwise turbulence along the ramp, measured with a single hot-wire, is shown at representative axial stations in figure 18(*a–d*). In each figure, contours of the pre-multiplied spectra $f'G_{u_s u_s}/U_\infty^2$ are presented, with the vertical axis showing the position in the boundary layer in terms of δ, and the horizontal axis showing the frequency normalized with the reference scale $f' = fD/U_\infty$. In general, the structure of the turbulence resonates with the character of the Reynolds stress profiles discussed in § 3.5. At all locations on the ramp, the most active region, across the frequency range, is centred about the outer turbulence peak that drifts further away from the wall downstream (following the dashed line from figure 18*a–d*). Consistent with the stress profiles the peak level reduces downstream, by approximately 30 %, from over 0.0025 upstream ($x/D = 2.297$) to just over 0.0018 at the BOR tail ($x/D = 3.172$). Furthermore, the approximate centroid of the active region shifts to lower frequency, sliding from $f' \sim 7$ at $x/D = 2.297$, figure 18(*a*), to $f' \sim 1.8$ at $x/D = 3.172$, figure 18(*d*), suggesting an amplification in the low-frequency motions in the outer region. This amplification of the large-scale motions can be visualized clearly by comparing the structure at each axial station, with that at a reference station, say at the BOR tail, as shown in figure 19. Here, the turbulence structure at various upstream stations (figure 18*a–c*) is scaled with that of the BOR tail (figure 18*d*), with the contour level representing the ratio of the spectra in dB scale. Compared with the BOR tail, the energy is generally weaker at low frequency (blue contours) but stronger at higher frequency (red contours). This difference intensifies upstream, with the maximum difference of the order of 10 dB at $x/D = 2.297$. For example, in figure 19(*a*), at $z - z_s = 0.25\delta$, the energy is lower for $f' < 2$ and higher for $f' > 2$, by over 10 dB. While this amplification of the large-scale motions is a generic feature of APG flows (Harun *et al.* 2013), the presence of lateral curvature is expected to further assist the amplification, as observed by Snarski & Lueptow (1995).

Figure 20(*a–d*) shows the turbulence structure plotted in terms of the ESL scaling. When the pre-multiplied spectra are plotted in the ESL coordinate system as $f'G_{u_s u_s}/U_d^2$ where $f' = f\delta_\omega/U_e$, the spectral structure appears similar along the ramp. Here, U_d is chosen as the velocity scale, δ_ω/U_e is chosen as the time scale since $U_e \propto U_d$ (3.6). The success of the ESL scaling was found to be superior to other related time scales δ/U_e, δ_1/U_e and δ/U_{zs}. The geometrical features are consistent, with the peak levels centred about

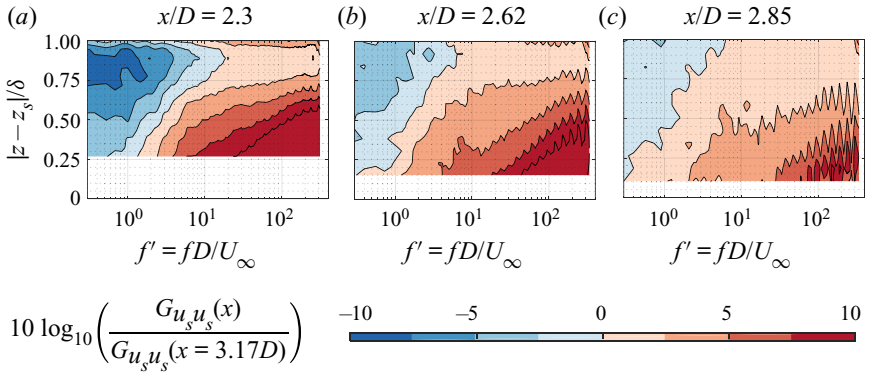

Figure 19. Comparison of the turbulence structure at various upstream stations, with that at the downstream BOR tail ($x/D = 3.172$). Contour levels represent the ratio of the pre-multiplied power spectrum to that at the BOR tail, on a dB scale; (*a*) $x/D = 2.297$, (*b*) $x/D = 2.615$, (*c*) $x/D = 2.854$.

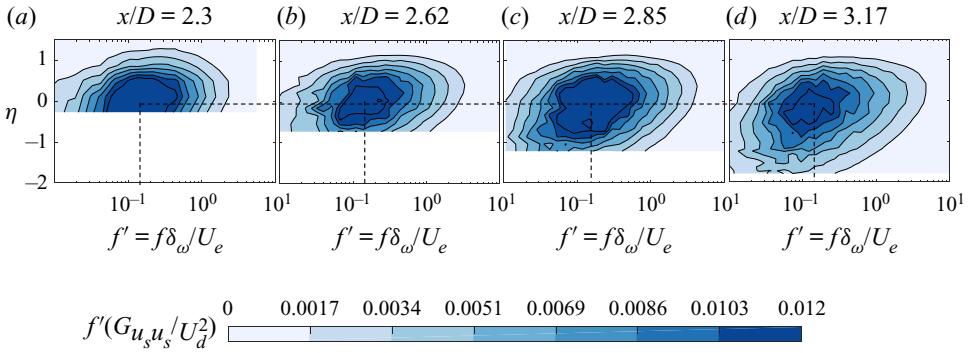

Figure 20. Contours of the pre-multiplied spectra of the streamwise velocity, $f' G_{u_s u_s}/U_d^2$, at different streamwise stations on the ramp. Frequency $f' = f\delta_\omega/U_e$, where $\delta_\omega(x)$ is vorticity thickness and $U_e(x)$ is edge velocity; (*a*) $x/D = 2.297$, (*b*) $x/D = 2.615$, (*c*) $x/D = 2.854$, (*d*) $x/D = 3.172$. Horizontal dashed lines indicate the position of the peak levels in the shear layer, and vertical dashed lines indicate the corresponding frequency of the peaks.

$\eta = 0$, and about frequency $f' = f\delta_\omega/U_e \sim 0.18$. The consistency along the ramp can be visualized better in figure 21. Similar to figure 19, the spectra at each station are normalized with the that of the BOR tail, with the contour levels representing the ratio of the spectra in dB scale. With the ESL scaling, the streamwise variations are typically within ± 2 dB as compared with ± 10 dB for the original spectra. Furthermore, for frequencies $f' < 1$ the streamwise variations are within ± 1 dB, corresponding to a $\pm 25\,\%$ change. This can be seen in the pre-multiplied line spectra extracted from the contours in figure 20, corresponding to various representative locations in terms of, η, shown for all streamwise locations on the ramp, in figure 22. While the functional form of the spectra changes with the distance from the wall, consistent with the expected inhomogeneity, the spectra from various streamwise stations are consistent at each η, particularly for $f' < 1$, suggesting that the low-frequency (large-scale) motions are consistent along the APG region. One can expect this from a boundary layer with an ESL, where the large-scale motions primarily driven by the shear layer are superposed on the underlying boundary layer turbulence.

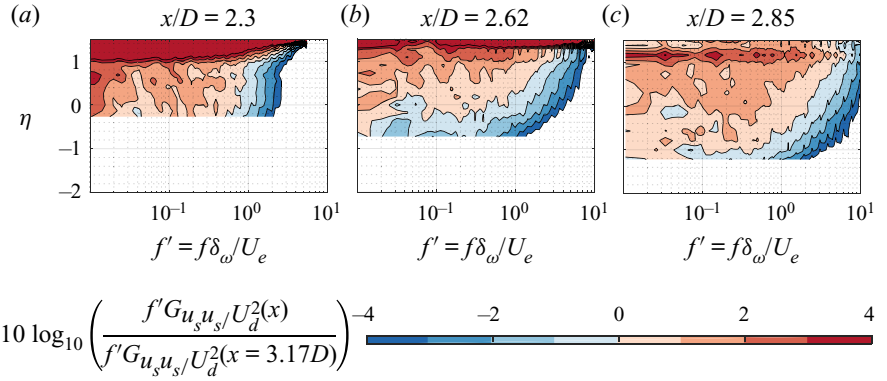

Figure 21. Contours of the pre-multiplied spectra of the streamwise velocity, $f'G_{u_su_s}/U_d^2$, at different streamwise stations on the ramp. Frequency $f' = f\delta_\omega/U_d$, where $\delta_\omega(x)$ is vorticity thickness and $U_e(x)$ is edge velocity; (*a*) $x/D = 2.297$, (*b*) $x/D = 2.615$, (*c*) $x/D = 3.172$.

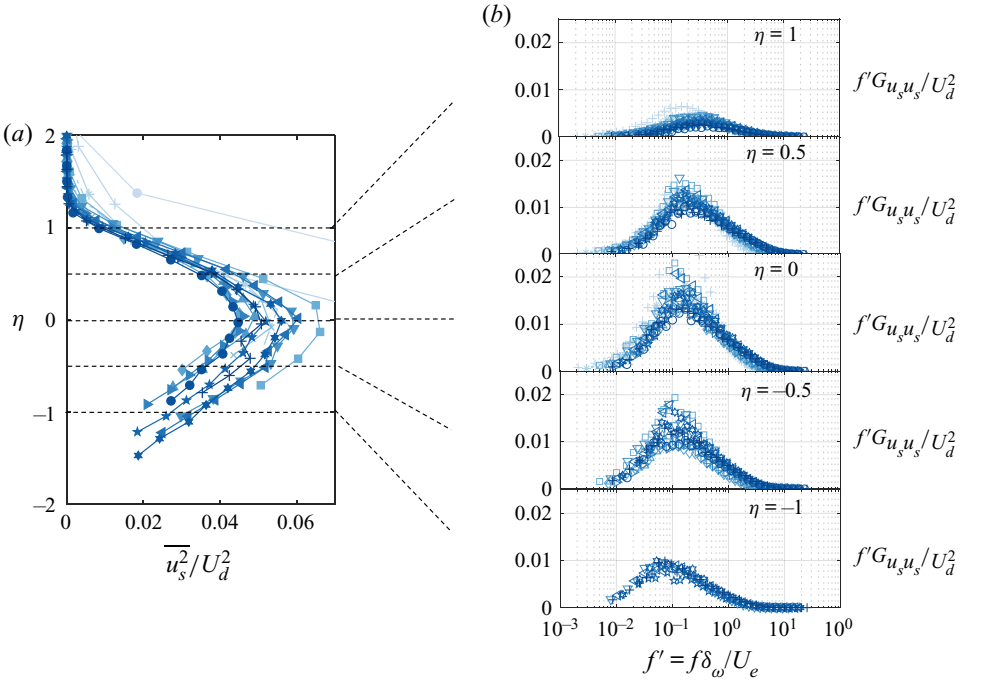

Figure 22. (*a*) Profiles of Reynolds stress with ESL scaling, showing the locations corresponding to the spectra to the right. (*b*) Pre-multiplied spectra of the streamwise velocity based on shear layer parameters. Line spectra in each plot are shown for a particular location in the shear layer based coordinate system. Line spectra shown for $\eta = -1, -0.5, 0, 0.5, 1$, moving from bottom to top. For legend refer to figure 14.

To summarize, the structure of streamwise turbulence is significantly modified by the strong APG and lateral curvature. The most active region continuously drifts higher in the boundary layer and is centred about the inflection point, consistent with the turbulence stress. As observed in previous studies, the importance of large-scale motions increases as they increasingly energize across the layer while small-scale motions weaken significantly.

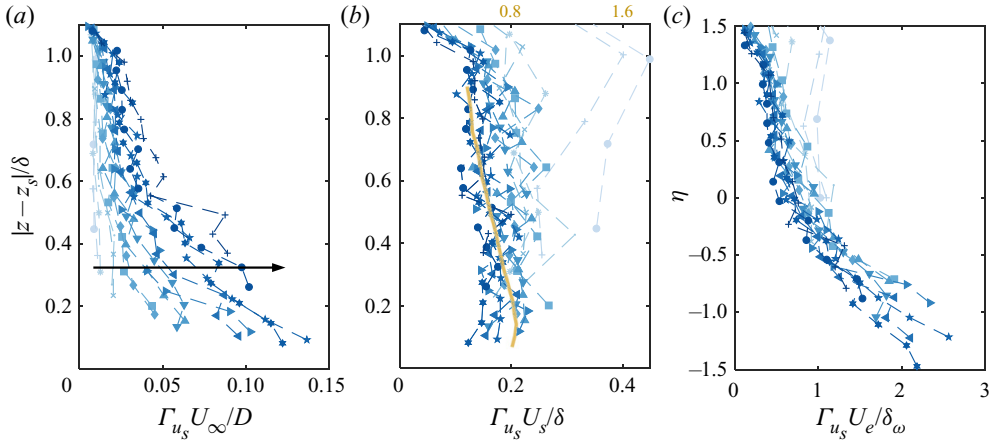

Figure 23. Integral time scales of the streamwise velocity, on the ramp boundary layer. (*a*) Integral time scales normalized on constant reference velocity and BOR diameter, black arrow shows the variation along the downstream direction. (*b*) Integral scales from (*a*) normalized on δ/U_s; orange curve represents the corresponding integral scales from a planar, zero pressure gradient boundary layer, at a $Re_{\delta_2} = 15\,000$ (Morton *et al.* 2012); corresponding *x*-axis shown on top. (*c*) Integral time scales normalized on the shear layer time scale (δ_ω/U_e). For legend see figure 14.

These large-scale motions appear to be driven by the ESL, with the spectrum below $f\delta_\omega/U_e < 1$ retaining its functional form along the ramp. Additionally, the performance of other scalings, based on the Zagarola–Smits velocity scale ($U_{zs} - \delta$) and on displacement thickness ($U_e - \delta_1$) was inferior to the ESL scaling. In the next section, the impact of APG on the spatial characteristics of the streamwise turbulence, including the evolution of length scales, two-point correlations and convection velocities are investigated.

3.7. *Correlation structure of streamwise velocity*

The integral time scale of the streamwise velocity on the ramp Γ_{u_s}, estimated from single hot-wire results, is shown in figure 23(*a*). The time scale is obtained by directly integrating the time-delay correlation coefficient ($\rho_{u_s u_s}$)

$$\Gamma_{u_s}(x, z) = \int_0^\infty \rho_{u_s u_s}(x, z, \tau)\,\mathrm{d}\tau, \tag{3.7}$$

where τ is the time delay. As seen in figure 23(*a*) the time scale increases moving into the boundary layer (for $|z - z_s| > 0.1\delta$) at all streamwise stations, and is consistent with both ZPG and APG studies in the past (Glegg & Devenport 2017; Lee 2017). Moving downstream along the ramp, the integral time scales – that represent large-scale motions – elongate as the mean flow expands, and at $|z - z_s| = 0.5\delta$ are approximately eight times longer at the BOR tail ($x/D = 3.172$) compared with upstream ($x/D = 2.059$). When normalized with the local boundary layer time scale δ/U_s (figure 23*b*) it can be seen that time scales grow roughly proportional to the boundary layer, and the overall form of the profile is somewhat preserved (within the uncertainty). Interestingly, this functional form resembles that of a planar, zero pressure gradient boundary layer at $Re_{\delta_2} \approx 15\,000$ (Morton, Devenport & Glegg 2012). While the organization is similar, the time scales of the BOR flow are approximately four times shorter than the ZPG layer, in proportion to the

respective δ/U_s, highlighting the importance of the pressure gradient and flow history. The integral time scales normalized on the ESL time scale (δ_ω/U_e) are shown in figure 23(c). The tighter collapse indicates the importance of the embedded shear layer motions in the boundary layer turbulence.

The corresponding streamwise integral length scales can be derived from the normalized time scale $\Gamma_{u_s}U_s/\delta$, shown in figure 23(b). In general, it is very common to estimate the turbulence length scales from single-point measurements such as described above. The typical assumption is to regard the turbulence as if it were frozen and convected by the mean flow, as hypothesized by Taylor (1938) for homogeneous and low turbulence flows. Several studies have investigated Taylor's hypothesis for wall-bounded flows (see Atkinson, Buchmann & Soria (2015); de Kat & Ganapathisubramani (2015) and Renard & Deck (2015) for ZPG boundary layers and Del Álamo & Jiménez (2009) for channel flow); both a scale-independent convection velocity (as a function of wall-normal location) and a comprehensive frequency-dependent velocity were developed and examined by these studies. A common finding for boundary layers has been that the convection velocity, for all scales, is nearly equal to the local mean speed except in the inner region, where the turbulence has been interpreted to travel significantly faster (Atkinson *et al.* 2015; Renard & Deck 2015). This is generally attributed to the amplitude modulation of near-wall turbulence by the outer, larger-scale turbulence (Mathis, Hutchins & Marusic 2009, 2011). While such observations appear to extend to moderate APG boundary layers over a flat plate (Drozdz & Elsner 2017), we are interested in briefly examining the convection velocity for the strongly decelerating BOR flow, towards the development of turbulence modelling and aeroacoustic predictions for vehicle-relevant configurations.

In order to examine Taylor's hypothesis for the BOR flow, we consider the comparisons between two-point spatial correlation from PIV measurements, and the single-point time-delay correlation from hot-wire measurements. In the following analysis, we will first introduce the two-point correlation function of the streamwise velocity in the BOR boundary layer, followed by a comparison with Taylor's hypothesis estimates of the correlation function, deduced from the single-point measurement. The comparisons will then be used to reveal the validity of Taylor's hypothesis, highlighting the importance of nonlinear effects due to the highly turbulent flow.

The two-point, spatial correlation coefficient for the streamwise velocity is defined as

$$\rho_{u_su_s}(x, z; x', z') = \frac{\langle u_s(x, z)u_s(x', z')\rangle}{\sqrt{\langle u_s^2(x, z)\rangle\langle u_s^2(x', z')\rangle}}, \tag{3.8}$$

where (x', z') is the reference location with respect to which the correlation is computed by averaging over time. For illustration, figure 24(a) shows the two-point correlation for a reference point at the BOR tail, located 0.56δ from the surface, corresponding to the outer peak in Reynolds stress. The horizontal and vertical axes are to scale in order to ensure accurate interpretation, and the contour lines radiate outward for every 0.1 drop in the correlation coefficient. The average eddy structure appears elliptic, with the major axis (connecting $\rho_{u_su_s} = 0.2$) inclined to the surface by 27°. While these geometric details are slightly sensitive to streamwise and radial position of the reference point, the structure is generally more compact (in proportion to δ) and further tilted from the horizontal in comparison with high Reynolds number ZPG layers (7°–12°) (Tutkun *et al.* 2009). This is consistent with our observation earlier in that the streamwise integral time scales of the BOR flow were four times shorter than the ZPG layer, in comparison with the respective δ.

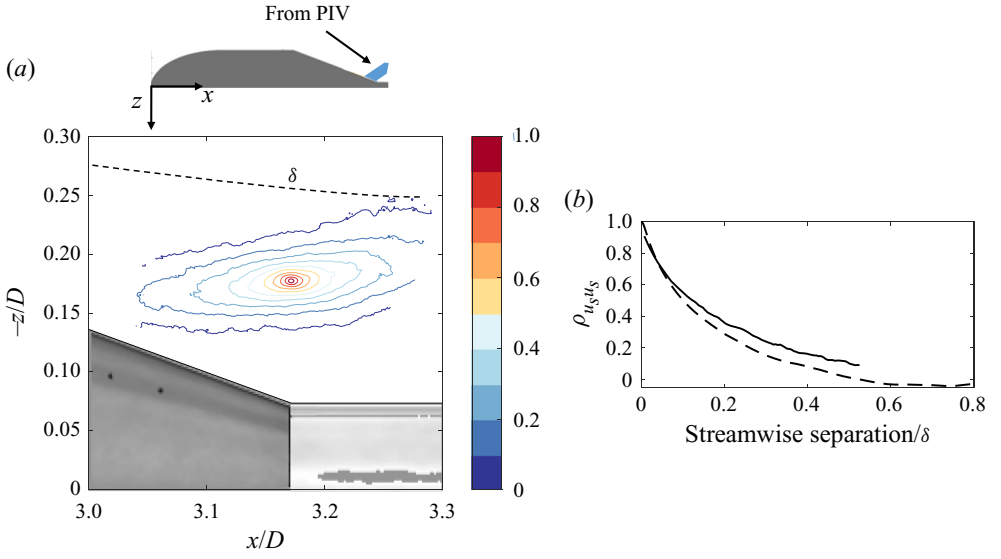

Figure 24. (*a*) Two-point correlation of the streamwise velocity from PIV, $\rho_{u_s u_s}(x', z'; x, z)$, with anchor point at $x'/D = 3.172$ and $z'/D = -0.177$ (corresponds to 0.56δ from surface). (*b*) Spatial correlation from (*a*) as a function of streamwise separation from PIV, (black line) $\rho_{T,u_s u_s}(x, z, \Delta x_s)$, compared with hot-wire estimates via Taylor's hypothesis (black dash) $\rho_{u_s u_s}(x', x' - U_s\tau)$.

A slice of the correlation structure from figure 24(*a*), drawn in the streamwise direction (in the direction of the local mean velocity) is shown in figure 24(*b*); this is compared with the single hot-wire estimate obtained through Taylor's hypothesis, defined as

$$\rho_{T,u_s u_s}(x', z'; \Delta x_s) = \frac{\langle u_s(x', z') u_s(x', z', x' - U_s\tau)\rangle}{\sqrt{\langle u_s^2(x', z')\rangle \langle u_s^2(x', z', x' - U_s\tau)\rangle}}, \tag{3.9}$$

where x', z' is the reference location (where the probe is positioned), $\Delta x_s (= x' - U_s\tau)$ is the separation along the streamwise direction, assuming that the turbulence is frozen and convecting at the local mean speed U_s. Clearly, the dashed line representing the Taylor's hypothesis estimate (3.9) decays faster than the solid line representing the two-point correlation from PIV (3.8), decaying to 10 % at 0.33δ, nearly twice as fast compared with 0.53δ for the two-point estimate. This inconsistency exists at all other streamwise stations, and there appears to be a definite pattern in the wall-normal direction to the inconsistency, as shown in figure 25. Here, the two-point correlation and Taylor's hypothesis estimate are compared for various locations in the boundary layer at a slightly upstream position ($x/D = 2.933$): while $\rho_{T,u_s u_s}(x', z', x' - U_s\tau)$ generally decays faster than the two-point estimates, the discrepancy intensifies further inside the boundary layer. To quantify this systematic deviation, we evaluate the integral length scales by numerically integrating the correlation coefficient (until the first zero crossing, using the trapezoidal rule), with the length scale obtained from PIV defined as,

$$L(x', z') = \int_0^\infty \rho(x', z', \Delta x_s)\, \mathrm{d}x_s. \tag{3.10}$$

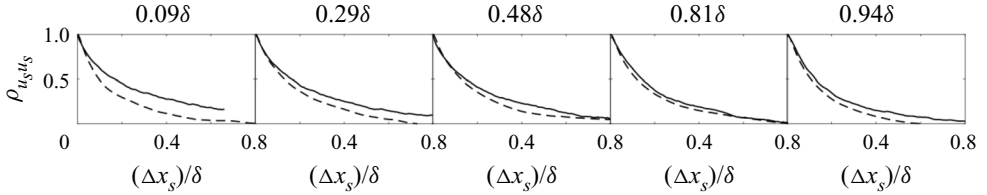

Figure 25. Two-point correlation from PIV (black line) compared with spatial correlation obtained from single-point hot-wire measurements (black dash) using Taylor's hypothesis, for $x/D = 2.933$.

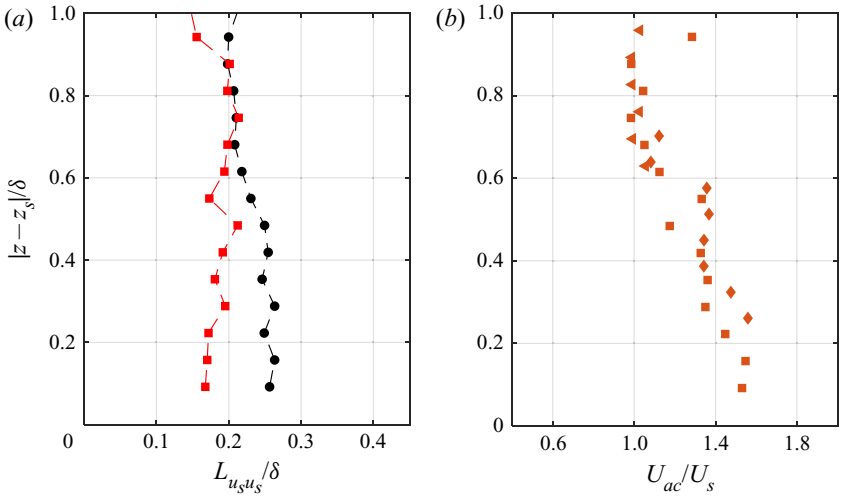

Figure 26. (*a*) Integral length scales in the boundary layer at $x/D = 2.933$; (black circle) $L_{u_s u_s}/\delta$ (PIV), (red square) $\Gamma_{u_s u_s} U_s/\delta$ (Taylor's hypothesis with local mean velocity). (*b*) Apparent convection velocity ($U_{ac} = L_{u_s u_s}/\Gamma_{u_s u_s}$) at representative streamwise stations; (orange triangleleft) $x/D = 2.854$; (orange square) $x/D = 2.933$; (orange diamond) $x/D = 3.092$.

And for the length scale estimate from time-delay correlations (through Taylor's hypothesis)

$$L_s(x', z') = \int_0^\infty \rho_T(x', z'; x' - U_s\tau)\,\mathrm{d}(x' - U_s\tau) = \Gamma(x', z')U_s(x', z'). \tag{3.11}$$

Estimates of the integral length scales at $x/D = 2.933$ obtained through (3.10)–(3.11) are shown in figure 26(*a*). Generally speaking, Taylor's hypothesis seems to reasonably predict the length scale in the outer half of the boundary layer ($>0.6\delta$), where we see PIV and hot-wire estimates are in agreement, at approximately 0.2δ. However, in the lower 40 % of the boundary layer, Taylor's hypothesis significantly underpredicts the length scale. Based on the local mean velocity, the length scale estimates are approximately 60 % smaller at $|z - z_s| = 0.1\delta$, suggesting that the nonlinear interactions play a significant role over distances much further from the wall than reported by ZPG flow studies. Therefore, significant corrections are required when estimating the length scale from single-point measurements, which is an important input for predictions of the far-field noise spectrum, for example of a rotor ingesting such highly turbulent flows. In this case, although an ingesting rotor sees the turbulence at a fixed location just like the fixed hot-wire, the

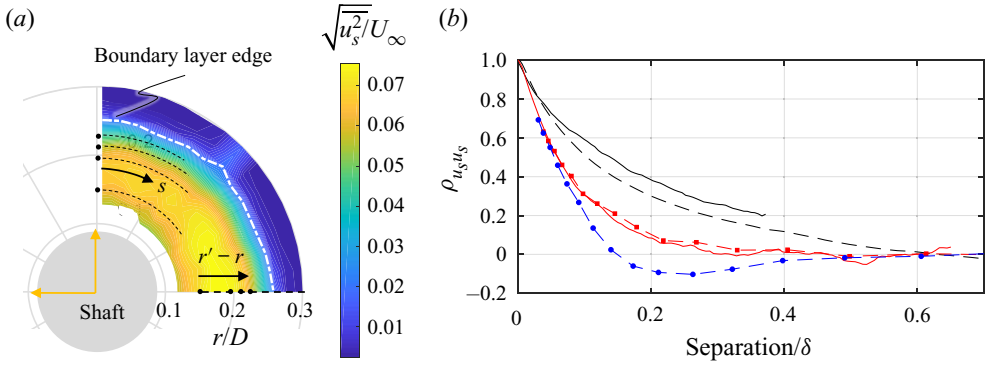

Figure 27. (*a*) The cross-section at BOR tail ($x/D = 3.172$), showing the measurement grid for circumferential and radial correlation measurements. Circumferential correlations are measured from the vertical axis and radial correlations along the horizontal axis. The contour levels in the background reveal the turbulence intensity. (*b*) Correlation coefficient of the streamwise velocity for an anchor point at 0.4δ at $x/D = 3.172$: solid lines indicate PIV results, dashed line indicate hot-wire results. Streamwise correlation in black, radial in red, and circumferential in blue.

fact that this inferred length scale is inaccurate may complicate the extrapolation of this estimate into the full multi-dimensional correlation function, increasing the error of using standard forms, such as from the homogeneous turbulence. To contain such a potential error, approximate corrections can be proposed, by assuming that the turbulence is still frozen as it convects, and estimating the apparent convection velocity (U_{ac}) of the integral turbulence structures, based on the measured length and time scales,

$$U_{ac}(x', z') = L_{u_s u_s}(x', z')/\Gamma_{u_s u_s}(x', z'). \tag{3.12}$$

The apparent convection velocity U_{ac} normalized on the local mean velocity, is shown in figure 26(*b*). Results are shown for available data at various stations along the tail, and the trends are approximately consistent across the stations. The frozen turbulence appears to convect at the local mean speed only in the outer portions of the boundary layer ($>0.6\delta$). Below 0.6δ, the convection velocity is over $1.4U_s$, as seen from the apparent convection velocity method. Closer to the wall, even significant corrections are expected. This is an important result for the aeroacoustics community.

To fully document the average eddy structure of streamwise velocity in order to provide quantitative inputs for turbulence modelling and aeroacoustic predictions, we measured a subset of the radial and circumferential correlations with a single hot-wire at the BOR tail ($x/D = 3.172$). With the conventional anchor-probe and moving-probe arrangement, the correlations were measured at four anchor points in the boundary layer, represented in figure 27(*a*) with the turbulence intensity contours in the background; while the circumferential correlations were measured about the vertical axis, the radial correlations were measured the horizontal, anchored at 0.40, 0.65, 0.75 and 0.85δ. As the trends were more or less consistent at all anchor points, results are shown for just the 0.4δ case in figure 27(*b*), along with the streamwise correlation for comparison. Here, the correlation coefficient $\rho_{u_s u_s}$ is shown on the vertical axis, with separation (normalized on δ) on the horizontal axis (separation implies $x' - x_s$ for streamwise, $r' - r$ for radial, $r'(\Delta\theta)$ for circumferential). Furthermore, to cross-validate measurements, the corresponding results from PIV (solid lines) are included with the hot-wire estimates (dashed lines): while the disagreement in the streamwise correlation has been attributed to the inaccuracy of

$-z/D$	$\lvert z-z_s\rvert/\delta$	$L_{u_su_s}(r)/\delta$	$L_{u_su_s}(c)/\delta$	L_r/L_c
0.147	0.40	0.089	0.060	1.48
0.194	0.65	0.081	0.055	1.47
0.212	0.75	0.079	0.055	1.44
0.231	0.85	0.078	0.043	1.80

Table 3. Integral length scales of the streamwise velocity, in the radial and circumferential directions, at the BOR tail ($x/D = 3.172$).

Taylor's hypothesis as discussed above, the agreement in the radial correlations suggests an absence of hot-wire probe interference effects.

Similar to the streamwise correlation, the radial correlation (red) decays monotonically with increasing separation, but decays approximately twice as fast, reaching 10 % level at a separation of 0.2δ. The circumferential correlations (blue) decay even faster, reaching 10 % level in approximately 0.12δ (depending slightly on the anchor position), and develop a negative tail (-5 %) at larger separation. The corresponding integral length scales, calculated by integrating the area under the correlation curve (including the negative excursions), and considered to represent the large-scale features, are shown in table 3 for the four anchor positions. Consistent with the correlations in figure 27(*b*) the radial length scale is 0.09δ, approximately 40 % of the streamwise length scale. The associated circumferential length scale at this position is even smaller at 0.06δ, roughly a quarter of the streamwise scale. This anisotropy of the length scales is not too different in the outer boundary layer as all the length scales shorten slightly, and are organized at a $1:0.6:0.3$ ratio (between the streamwise, radial and circumferential scales) at 0.85δ.

4. Conclusions

This study describes the experiments performed over a BOR at a Reynolds number, based on the length and free-stream velocity, of 1.9 million. The transverse curvature parameters were moderate ($\delta/r_s < 2$, $r_s^+ > 500$), while the pressure gradient was increasingly adverse towards the tail ($\beta_C \to 5, 20$); representative of the vehicle-relevant conditions with axially varying curvature and pressure gradient. The dataset for this non-equilibrium boundary layer is publicly available from doi: https://doi.org/10.7294/16655860.

The combined response to the APG and the transverse curvature is evaluated on the mean flow, turbulence structure and correlation structure. Important results include:

(i) The mean-velocity and turbulence intensity profiles appear self-similar with the embedded shear layer scaling (Schatzman & Thomas 2017). Based on the inflection points in the boundary layer, located at $1.2\times$ displacement thickness from the surface, the velocity defect served as the velocity scale while the vorticity thickness served as the length scale. The functional form of the velocity profile was well described by error function (commonly used for planar mixing layer flows). While the collapse in the turbulence intensity was not as strong, the peak turbulent stress is approximately $0.23U_d$, close to the value of $0.21U_d$ observed by Schatzman & Thomas.

(ii) The vorticity thickness was found to grow linearly along the streamwise direction, at a rate consistent with free-shear layer flows. Furthermore, the length and velocity scales were found to be directly proportional to the boundary layer edge velocity and

thickness, respectively, by a factor of 0.4. However, it is not definitive whether the inviscid instabilities drive the ESL motions, and further investigation is necessary to determine if the existence of mean-velocity inflection points and the ESL are correlated but not causal.

(iii) The turbulence structure of the streamwise velocity reflects the observations from the mean flow. The flow becomes increasingly turbulent, with the large-scale motions amplifying and grow roughly proportional to the boundary layer thickness. In the low-frequency regions, the pre-multiplied spectra scale with the embedded shear layer time scale (δ_ω/U_e), emphasizing the direct influence of the ESL motions in the large-scale activity.

(iv) Analysis of the correlation structure revealed that the nonlinear interactions in the turbulence could be significant since Taylor's hypothesis severely underpredicted the integral length scales. Comparisons of the two-point correlations from PIV and the single-point estimates (from a single hot-wire, using Taylor's hypothesis) revealed that the apparent convection velocity is approximately 1.4 times the local mean velocity in the inner half of the boundary layer, and even higher close to the wall. These corrections must be factored in when single-point measurements are used to derive the length scales, which is a common practice in the aeroacoustics far-field noise predictions.

Acknowledgments. We acknowledge the support from the Office of Naval Research. We are grateful to Drs S. Glegg, M. Wang, W. Blake and J. Anderson, and Mr M. Marcolini, for their helpful advice and support on this work. We wish to thank the Aerospace and Ocean Engineering Machine Shop staff headed by Mr J. Lambert, in leading the fabrication and instrumentation hardware efforts. We also thank the Virginia Tech Wind Tunnel staff Dr A. Borgoltz, Mr B. Oetjens; and all the graduate research assistants, particularly Mr A. Millican, for assistance during experiments. We wish to thank the three anonymous reviewers for their insightful suggestions. We also appreciate Professor Y. Maciel for providing the DNS2017 dataset from Maciel *et al.* (2018).

Funding. This work is supported by funding from Office of Naval Research with program managers, K.-H. Kim and J. Muench under grants N00014-17-1-2698 and N00014-20-1-2650.

Declaration of interests. The authors report no conflict of interest.

Data availability statement. The dataset for the non-equilibrium boundary layer is publicly available from doi: https://doi.org/10.7294/16655860.

Author ORCIDs.
N. Agastya Balantrapu https://orcid.org/0000-0002-5641-4566.

Appendix A. Cross-validation of velocity statistics

This appendix contains a comparison of the velocity statistics obtained through various measurement methods. Profiles of the streamwise mean velocity and turbulence intensity are shown for three representative stations in figure 28(*a–f*) comparing the results from single hot-wire anemometry, four-sensor hot-wire anemometry and planar PIV. The deviations across different methods are minor (for example the turbulence intensities from PIV are within 7 % of the hot-wire estimates) and do not impact the analysis and conclusions of the work. Note that the turbulence intensity from four-sensor hot-wire are excluded from the comparisons due to significant errors expected from rectification and gradient errors (Tutu & Chevray 1975) due to a highly turbulent flow as a result of a strong APG and are excluded from the paper altogether.

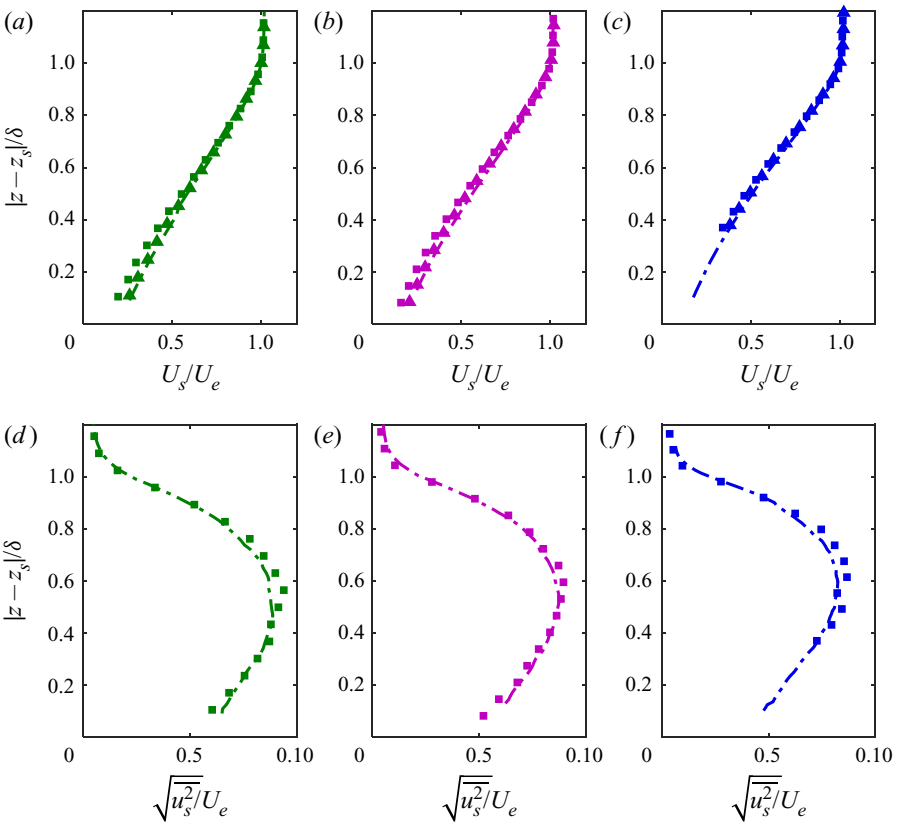

Figure 28. Profiles of streamwise mean velocity (*a–c*) and turbulence intensity (*d–f*) comparing the results from various measurement methods: PIV (black dash dot), single hot-wire (black square), four-sensor hot-wire (black triangleup), at representative stations along the tail: $x/D = 2.854$ (green), $x/D = 3.013$ (magenta), $x/D = 3.172$ (blue) (see figure 9 for relative locations and table 2 for boundary layer parameters).

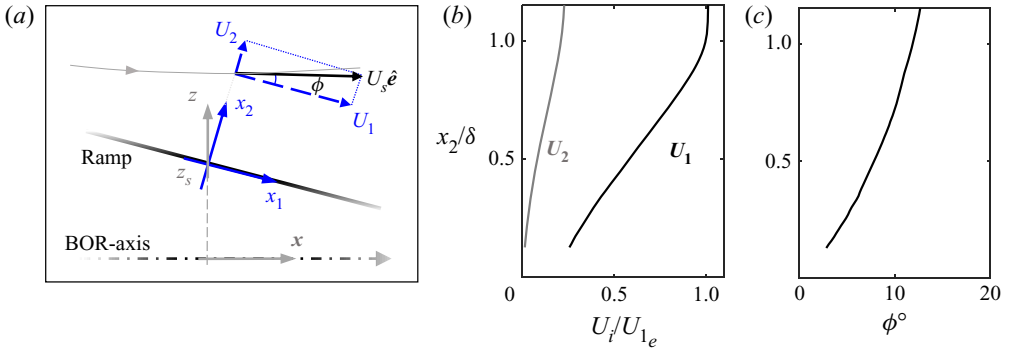

Figure 29. (*a*) Schematic of the coordinate frames to analyse the boundary layer statistics, with the x–z system (in grey) as used throughout the paper, and the boundary layer coordinate frame $x_1 - x_2$ (in blue). Note that the grey line with an arrow illustrates a streamline with the U_s implying the mean streamwise velocity. Also, the flow angle ϕ has been exaggerated for clarity. (*b*) Profiles of the velocity components resolved in the boundary layer coordinate frame, for a sample station along the tail at $x/D = 3.013$. (*c*) Orientation of the mean flow with respect to the surface as function of the wall-normal position, corresponding to (*b*).

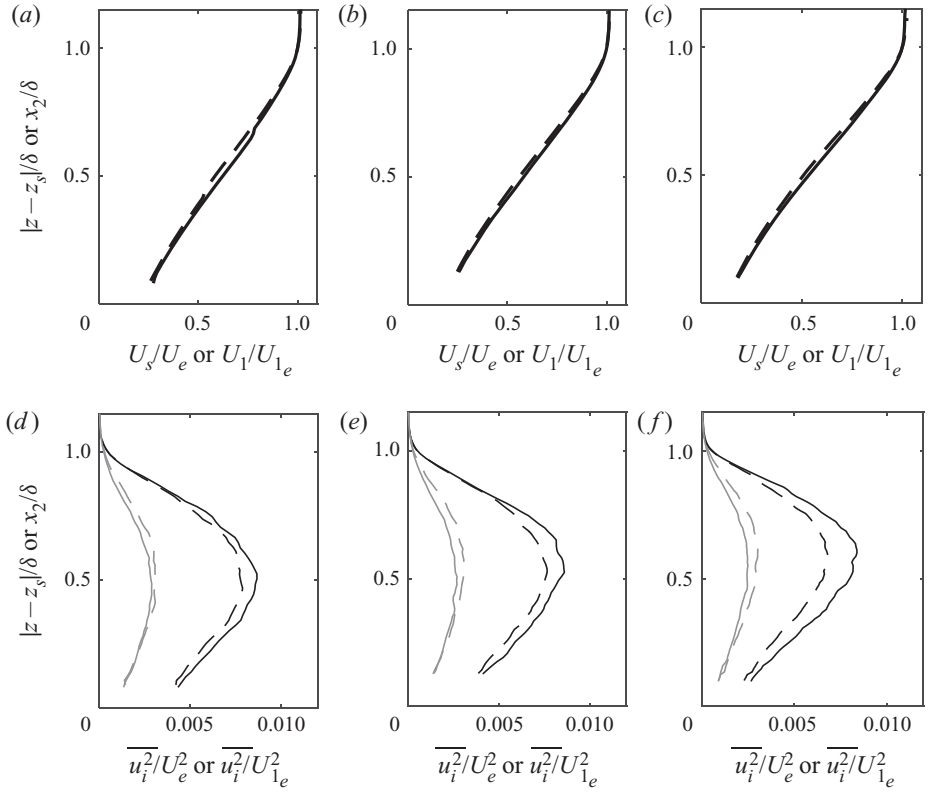

Figure 30. Comparison of the velocity statistics in the radial–streamwise coordinate frame adopted in the paper with those in the boundary layer coordinate frame, for multiple stations on the BOR tail. (*a–c*) Show the mean-velocity profiles at $x/D = 2.854, 3.013, 3.172$, respectively, while (*d–f*) show the corresponding Reynolds normal stresses. Solid lines show the results in the boundary layer frame (wall-normal profiles of the velocity in the wall coordinate system, see figure 29) while dashed lines show the corresponding radial profiles of the velocity resolved in the streamwise-oriented coordinate system. Additionally, in (*d–f*) the black and grey solid lines show u_1^2/U_e^2 and u_2^2/U_e^2, respectively, while black and grey dashed lines represent u_s^2/U_e^2 and u_n^2/U_e^2, respectively.

Appendix B. Impact of the coordinate frame on analysis

In this appendix we present the impact of the coordinate frame chosen throughout the analysis and discussion in §§ 3.3–3.7, using the PIV results recast in the conventional boundary layer coordinate system. Figure 29(*a*) shows both coordinate frames; the first one, used throughout the paper, is the x–z (axial–radial) system where profiles of the streamwise velocity (U_s) were measured by radially traversing the single hot-wire from the surface. The second frame $x_1 - x_2$ is the boundary layer coordinate system, with x_1 and x_2 measured along and normal to the surface, respectively, with U_1 and U_2 representing the corresponding velocity components. Figure 29(*b*,*c*) shows the resulting profiles of the velocity components and flow angle relative to the surface, for a representative station at $x/D = 3.013$; the flow orientation with respect to the wall changes significantly across the boundary layer and is approximately 12° in the local free stream, and this changes along the tail. Philosophically, we think this dilutes the $U_1 \gg U_2$ assumption of the boundary layer theory, allowing some freedom into the selection of an equally physically meaningful coordinate frame, as we have chosen. In such a case, it is important to observe

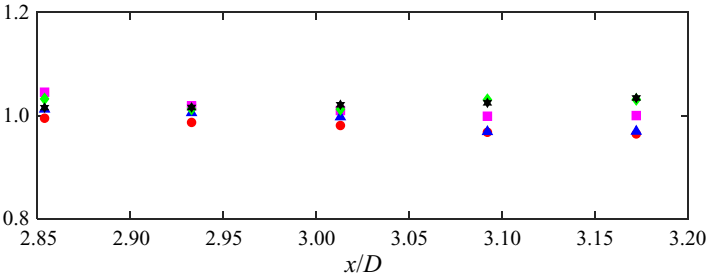

Figure 31. Ratio of boundary layer parameters in the radial system to those obtained in the boundary layer frame: (red circle) δ; (magenta square) δ_1; (blue triangleup) δ_2; (black hexagon) U_e; (green diamond) $H = \delta_1/\delta_2$.

the consequences of choosing such a frame, in order to ensure interpretation as it relates to the boundary layer coordinate system and to facilitate comparisons with the literature. We address this issue below, by comparing the results in either coordinate systems by transforming the PIV data from multiple streamwise stations along the tail. It is shown that the results and discussion are generally unaffected by the coordinate frame, and the estimated boundary layer parameters are consistent to within 5 %, which is of the order of the expected uncertainty.

Figure 30 shows a comparison of the velocity statistics for multiple locations along the tail, with figure 30(*a–c*) containing the mean velocity and (*d–f*) containing Reynolds normal stresses. While solid lines represent the results in boundary layer system ($x_1 - x_2$), dashed lines represent profiles oriented radially outward ($|z - z_s|$) with the velocity in the streamwise direction as used in §§ 3.3–3.7. While the mean velocity profiles are consistent with each other at all shown locations, there seem to be some offset (10 %–20 %) in the Reynolds normal stresses which were found to arise primarily due to the rotation of the stress tensor into the wall-oriented coordinate system from the streamwise system, and were not sensitive to whether the profile was wall-normal or radially oriented. While this marginally improves the collapse of the profiles such as shown in figure 14, this does not alter the analysis and conclusions of this work. Additionally, the boundary layer parameters estimated from either coordinate systems are consistent to within 5 %, as shown in figure 31. Similarly, it was found that the other important parameters such as the location of the Reynolds stress peak normalized on δ_1, and the ESL parameters shown in (3.6) were not sensitive to the choice of the coordinate frame.

References

Atkinson, C., Buchmann, N.A., Amili, O. & Soria, J. 2013 On the appropriate filtering of PIV measurements of turbulent shear flows. *Exp. Fluids* **55** (1), 1654.

Atkinson, C., Buchmann, N.A. & Soria, J. 2015 An experimental investigation of turbulent convection velocities in a turbulent boundary layer. *Flow Turbul. Combust.* **94** (1), 79–95.

Bearman, P.W. 1971 Corrections for the effect of ambient temperature drift on hot-wire measurements in incompressible flow. *DISA Inform.* **11**, 25–30.

Bobke, A., Vinuesa, R., Örlü, R. & Schlatter, P. 2017 History effects and near equilibrium in adverse-pressure-gradient turbulent boundary layers. *J. Fluid Mech.* **820**, 667–692.

Castillo, L. & George, W.K. 2001 Similarity analysis for turbulent boundary layer with pressure gradient: outer flow. *AIAA J.* **39** (1), 41–47.

Cipolla, K.M. & Keith, W.L. 2003 High Reynolds number thick axisymmetric turbulent boundary layer measurements. *Exp. Fluids* **35** (5), 477–485.

Clauser, F.H. 1954 Turbulent boundary layer in adverse pressure gradient. *J. Aero. Sci.* **21**, 91–108.

DE KAT, R. & GANAPATHISUBRAMANI, B. 2015 Frequency–wavenumber mapping in turbulent shear flows. *J. Fluid Mech.* **783**, 166–190.

DEL ÁLAMO, J.C. & JIMÉNEZ, J. 2009 Estimation of turbulent convection velocities and corrections to Taylor's approximation. *J. Fluid Mech.* **640**, 5–26.

DENGEL, P. & FERNHOLZ, H.H. 1990 An experimental investigation of an incompressible turbulent boundary layer in the vicinity of separation. *J. Fluid Mech.* **212**, 615–636.

DEVENPORT, W.J., BURDISSO, R.A., BORGOLTZ, A., RAVETTA, P.A., BARONE, M.F., BROWN, K.A. & MORTON, M.A. 2013 The Kevlar-walled anechoic wind tunnel. *J. Sound Vib.* **332** (17), 3971–3991.

DROZDZ, A. & ELSNER, W. 2017 Amplitude modulation and its relation to streamwise convection velocity. *Intl J. Heat Fluid Flow* **63**, 67–74.

ELSBERRY, K, LOEFFLER, J, ZHOU, M.D. & WYGNANSKI, I 2000 An experimental study of a boundary layer that is maintained on the verge of separation. *J. Fluid Mech.* **423**, 227–261.

GLAUERT, M.B. & LIGHTHILL, M.J. 1955 The axisymmetric boundary layer on a long thin cylinder. *Proc. R. Soc. Lond.* A **230** (1181), 188–203.

GLEGG, S. & DEVENPORT, W. 2017 *Aeroacoustics of Low mach Number Flows: Fundamentals, Analysis, and Measurement*. Academic Press.

GUNGOR, A.G., MACIEL, Y., SIMENS, M.P. & SORIA, J. 2016 Scaling and statistics of large-defect adverse pressure gradient turbulent boundary layers. *Intl J. Heat Fluid Flow* **59**, 109–124.

HAMMACHE, M., BROWAND, F.K. & BLACKWELDER, R.F. 2002 Whole-field velocity measurements around an axisymmetric body with a Stratford–Smith pressure recovery. *J. Fluid Mech.* **461**, 1–24.

HARUN, Z., MONTY, J.P., MATHIS, R. & MARUSIC, I. 2013 Pressure gradient effects on the large-scale structure of turbulent boundary layers. *J. Fluid Mech.* **715**, 477–498.

HUANG, T., LIU, H.L., GROVES, N., FORLINI, T., BLANTON, J. & GOWLING, S. 1992 Measurements of flows over an axisymmetric body with various appendages in a wind tunnel: the DARPA SUBOFF experimental program. In *Proceedings of the 19th Symposium of Naval HYDRODYNAMICS*, Session V, p. 321. National Academy Press.

HUTCHINS, N., NICKELS, T.B., MARUSIC, I. & CHONG, M.S. 2009 Hot-wire spatial resolution issues in wall-bounded turbulence. *J. Fluid Mech.* **635**, 103–136.

JIMENEZ, J.M., HULTMARK, M. & SMITS, A.J. 2010 The intermediate wake of a body of revolution at high Reynolds numbers. *J. Fluid Mech.* **659**, 516–539.

JORDAN, S.A. 2014 On the axisymmetric turbulent boundary layer growth along long thin circular cylinders. *Trans. ASME J. Fluids Engng* **136** (5), 051202.

KITSIOS, V., SEKIMOTO, A., ATKINSON, C., SILLERO, J.A., BORRELL, G., GUNGOR, A.G., JIMÉNEZ, J. & SORIA, J. 2017 Direct numerical simulation of a self-similar adverse pressure gradient turbulent boundary layer at the verge of separation. *J. Fluid Mech.* **829**, 392–419.

KUMAR, P. & MAHESH, K. 2018*a* Analysis of axisymmetric boundary layers. *J. Fluid Mech.* **849**, 927–941.

KUMAR, P. & MAHESH, K. 2018*b* Large-eddy simulation of flow over an axisymmetric body of revolution. *J. Fluid Mech.* **853**, 537–563.

LEE, J.H. 2017 Large-scale motions in turbulent boundary layers subjected to adverse pressure gradients. *J. Fluid Mech.* **810**, 323–361.

LEE, J.H., KEVIN, MONTY, J.P. & HUTCHINS, N. 2016 Validating under-resolved turbulence intensities for PIV experiments in canonical wall-bounded turbulence. *Exp. Fluids* **57** (8), 129.

LUEPTOW, R.M., LEEHEY, P. & STELLINGER, T. 1985 The thick, turbulent boundary layer on a cylinder: mean and fluctuating velocities. *Phys. Fluids* **28** (12), 3495–3505.

MACIEL, Y., SIMENS, M.P. & GUNGOR, A.G. 2017 Coherent structures in a non-equilibrium large-velocity-defect turbulent boundary layer. *Flow Turbul. Combust.* **98** (1), 1–20.

MACIEL, Y., TIE, W., GUNGOR, A.G. & SIMENS, M.P. 2018 Outer scales and parameters of adverse-pressure-gradient turbulent boundary layers. *J. Fluid Mech.* **844**, 5–35.

MANOVSKI, P., GIACOBELLO, M. & JACQUEMIN, P. 2014 Smoke flow visualisation and particle image velocimetry measurements over a generic submarine model. *Tech. Rep.*. Defence Science and Technology Organization (Australia).

MANOVSKI, P., JONES, M.B., HENBEST, S.M., XUE, Y., GIACOBELLO, M. & DE SILVA, C. 2020 Boundary layer measurements over a body of revolution using long-distance particle image velocimetry. *Intl J. Heat Fluid Flow* **83**, 108591.

MATHIS, R., HUTCHINS, N. & MARUSIC, I. 2009 Large-scale amplitude modulation of the small-scale structures in turbulent boundary layers. *J. Fluid Mech.* **628**, 311–337.

MATHIS, R., HUTCHINS, N. & MARUSIC, I. 2011 A predictive inner–outer model for streamwise turbulence statistics in wall-bounded flows. *J. Fluid Mech.* **681**, 537–566.

MICHALKE, A. 1991 On the instability of wall-boundary layers close to separation. In *Separated Flows and Jets* (ed. V.V. Kozlov & A.V. Dovgal), pp. 557–564. Springer Berlin Heidelberg.

MORTON, M.A., DEVENPORT, W.J. & GLEGG, S. 2012 Rotor inflow noise caused by a boundary layer: inflow measurements and noise predictions. In *18th AIAA/CEAS Aeroacoustics Conference (33rd AIAA Aeroacoustics Conference)*, p. 2120. American Institute of Aeronautics and Astronautics.

NAGANO, Y., TSUJI, T. & HOURA, T. 1998 Structure of turbulent boundary layer subjected to adverse pressure gradient. *Intl J. Heat Fluid Flow* **19** (5), 563–572.

NEVES, J.C., MOIN, P. & MOSER, R.D. 1994 Effects of convex transverse curvature on wall-bounded turbulence. Part 1. The velocity and vorticity. *J. Fluid Mech.* **272**, 349–382.

OSTER, D. & WYGNANSKI, I. 1982 The forced mixing layer between parallel streams. *J. Fluid Mech.* **123**, 91–130.

PATEL, V.C., NAKAYAMA, A & DAMIAN, R 1974 Measurements in the thick axisymmetric turbulent boundary layer near the tail of a body of revolution. *J. Fluid Mech.* **63** (2), 345–367.

PIQUET, J. & PATEL, V.C. 1999 Transverse curvature effects in turbulent boundary layer. *Prog. Aero. Sci.* **35** (7), 661–672.

POPE, S.B. 2001 *Turbulent Flows*. Cambridge University Press.

RAFFEL, M., WILLERT, C.E., SCARANO, F., KÄHLER, C.J., WERELEY, S.T. & KOMPENHANS, J. 2018 *Particle image velocimetry: a practical guide*. Springer.

RAO, G.N.V. 1967 The law of the wall in a thick axisymmetric turbulent boundary layer. *J. Appl. Mech.* **34** (1), 237–238.

RENARD, N. & DECK, S. 2015 On the scale-dependent turbulent convection velocity in a spatially developing flat plate turbulent boundary layer at Reynolds number $Re_\theta = 13\,000$. *J. Fluid Mech.* **775**, 105–148.

SCHATZMAN, D.M. & THOMAS, F.O. 2017 An experimental investigation of an unsteady adverse pressure gradient turbulent boundary layer: embedded shear layer scaling. *J. Fluid Mech.* **815**, 592–642.

SCHETZ, J.A & BOWERSOX, R.D.W. 2011 *Boundary layer analysis*. American Institute of Aeronautics and Astronautics.

SKÅRE, P.E. & KROGSTAD, P. 1994 A turbulent equilibrium boundary layer near separation. *J. Fluid Mech.* **272**, 319–348.

SNARSKI, S.R. & LUEPTOW, R.M. 1995 Wall pressure and coherent structures in a turbulent boundary layer on a cylinder in axial flow. *J. Fluid Mech.* **286**, 137–171.

SONG, S., DEGRAAFF, D.B. & EATON, J.K. 2000 Experimental study of a separating, reattaching, and redeveloping flow over a smoothly contoured ramp. *Intl J. Heat Fluid Flow* **21** (5), 512–519.

TAYLOR, G.I. 1938 The spectrum of turbulence. *Proc. R. Soc. Lond.* A **164** (919), 476–490.

TUTKUN, M., GEORGE, W.K., DELVILLE, J., STANISLAS, M., JOHANSSON, P.B.V., FOUCAUT, J.M. & COUDERT, S. 2009 Two-point correlations in high Reynolds number flat plate turbulent boundary layers. *J. Turbul.* **10**, N21.

TUTTY, O.R. 2008 Flow along a long thin cylinder. *J. Fluid Mech.* **602**, 1–37.

TUTU, N.K. & CHEVRAY, R. 1975 Cross-wire anemometry in high intensity turbulence. *J. Fluid Mech.* **71** (4), 785–800.

VILA, C.S., ÖRLÜ, R., VINUESA, R., SCHLATTER, P., IANIRO, A. & DISCETTI, S. 2017 Adverse-pressure-gradient effects on turbulent boundary layers: statistics and flow-field organization. *Flow Turbul. Combust.* **99** (3–4), 589–612.

WITTMER, K.S., DEVENPORT, W.J. & ZSOLDOS, J.S. 1998 A four-sensor hot-wire probe system for three-component velocity measurement. *Exp. Fluids* **24** (5), 416–423.

WYGNANSKI, I., CHAMPAGNE, F. & MARASLI, B. 1986 On the large-scale structures in two-dimensional, small-deficit, turbulent wakes. *J. Fluid Mech.* **168**, 31–71.

ZAGAROLA, M.V. & SMITS, A.J. 1998 Mean-flow scaling of turbulent pipe flow. *J. Fluid Mech.* **373**, 33–79.

ZHOU, D., WANG, K. & WANG, M. 2020 Large-eddy simulation of an axisymmetric boundary layer on a body of revolution. In *AIAA Aviation 2020 Forum*, p. 2989. American Institute of Aeronautics and Astronautics.